Materials & Design 241 (2024) 112916

Contents lists available at ScienceDirect

Materials & Design

journal homepage: www.elsevier.com/locate/matdes

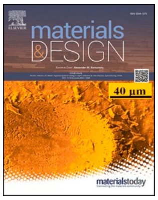

Enhancing the fracture properties of carbon fiber-calcium silicate hydrate interface through graphene oxide

Benzhi Min [a,1], Guoliang Chen [b,1], Yongyang Sun [a], Ke Li [c], Xi Chen [d], Zhenqing Wang [a,*]

[a] *College of Aerospace and Civil Engineering, Harbin Engineering University, Harbin 150001, China*
[b] *School of Energy Science and Engineering, Harbin Institute of Technology, Harbin 150001, China*
[c] *Institute of Materials Research and Engineering (IMRE), Agency for Science, Technology and Research (A*STAR), 2 Fusionopolis Way, Innovis #08-03, Singapore 138634, Singapore*
[d] *School of Materials Science and Engineering, Nanyang Technological University, 639798, Singapore*

ABSTRACT

As a quasi-brittle material, concrete's toughness and durability are significantly affected by cracking. Extensive research has been focused on fiber reinforcing, a popular way to enhance concrete's mechanical properties. The bonding performance of the fiber–matrix interface plays a critical role in determining overall compatibility and microcrack formation. In this study, A series of all-atom models of the interface between carbon fibers (CF) and calcium silicate hydrates (C-S-H) were established and molecular dynamics simulations was used to investigate fiber pullout and uniaxial tensile response in the matrix. By incorporating graphene oxide (GO) sheets within the interface, the damage strength and critical energy release rate of the C-S-H and carbon fibers interface were significantly improved, with increases of 22.64% to 63.81% and 37.18% to 43.90%, respectively. Furthermore, the role of hydrogen bonding and interatomic interactions in resisting interfacial damage is clarified with delving into the intermolecular interactions inside the interface. Our study offers atomic-level insights into how nano-additives can enhance the mechanical performance of fiber-reinforced concrete (FRC), providing new ideas for the "bottom-up" design of high-performance concrete.

1. Introduction

Concrete is the most widely used building material in the world [1,2], while the share of carbon dioxide generated by its production and manufacturing processes in the global energy-related sector is increasing every year [3]. To mitigate its environmental impact, researchers are focused on developing concrete with superior performance, which can reduce the carbon footprint of cement [4,5]. Nevertheless, an increase in compressive strength often leads to brittleness under tensile or flexural load. In complex loading and environmental situations, such as in dam structures, highly brittle and low-toughness plain concrete (PC) cannot fulfill the requirements for better safety [6]. To address this, fiber-reinforced cementitious composites are gaining scholarly attention as they offer improved ductility. Popular fiber materials such as steel fibers, polyvinyl alcohol (PVA) fibers, basalt fibers, and carbon fibers are often used in fiber-reinforced concrete (FRC) [7–9]. Among these fibers, carbon fibers stand out due to their exceptional tensile strength, modulus, and corrosion resistance. Incorporating a small amount of blended carbon fibers can significantly enhance the tensile strength and energy absorption capacity of concrete [10,11]. Multiple cracks smaller than in ordinary concrete can be observed during the damage process of FRC [12], which is due to the role of fibers in bridging cracks, deflecting crack paths, and blunting crack tips, thereby resisting crack expansion [13,14]. Consequently, the bond strength between fibers and the matrix plays a vital role in determining the extent of concrete's improved strength and toughness [15–18]. The interfacial transition zone (ITZ) between the matrix and the fiber is a crucial factor affecting the bond strength, underscoring the necessity for a deeper understanding of the matrix-fiber interface to design higher performance FRCs.

The interfacial transition zone in ordinary concrete mainly comprises ettringite (AFt), calcium hydroxide (CH) crystals, and calcium silicate hydrate (C-S-H) gels, with widths ranging from 20 μm to 100 μm [19,20]. The microstructure of FRC is notably more intricate due to the presence of the ITZ between fibers and the matrix [21]. Given that local cracks and failures often initiate within the ITZ, further research on improving the fracture toughness of fiber–matrix interface is imperative [22]. At microscale, nano-additives have emerged as popular ways to reinforcing concrete on the basis of fiber reinforcement, by reducing defects and improving interfacial bonding properties at the microscopic scale [23,24]. The nucleation, filling and binding effects between C-S-H nanoparticles and nano-additives, coupled with their high specific area, significantly reduce the capillary porosity within the interface and

---

[*] Corresponding author.
E-mail address: wangzhenqing@hrbeu.edu.cn (Z. Wang).
[1] These authors contributed equally to this work and should be considered co-first authors.

https://doi.org/10.1016/j.matdes.2024.112916
Received 11 October 2023; Received in revised form 19 March 2024; Accepted 3 April 2024

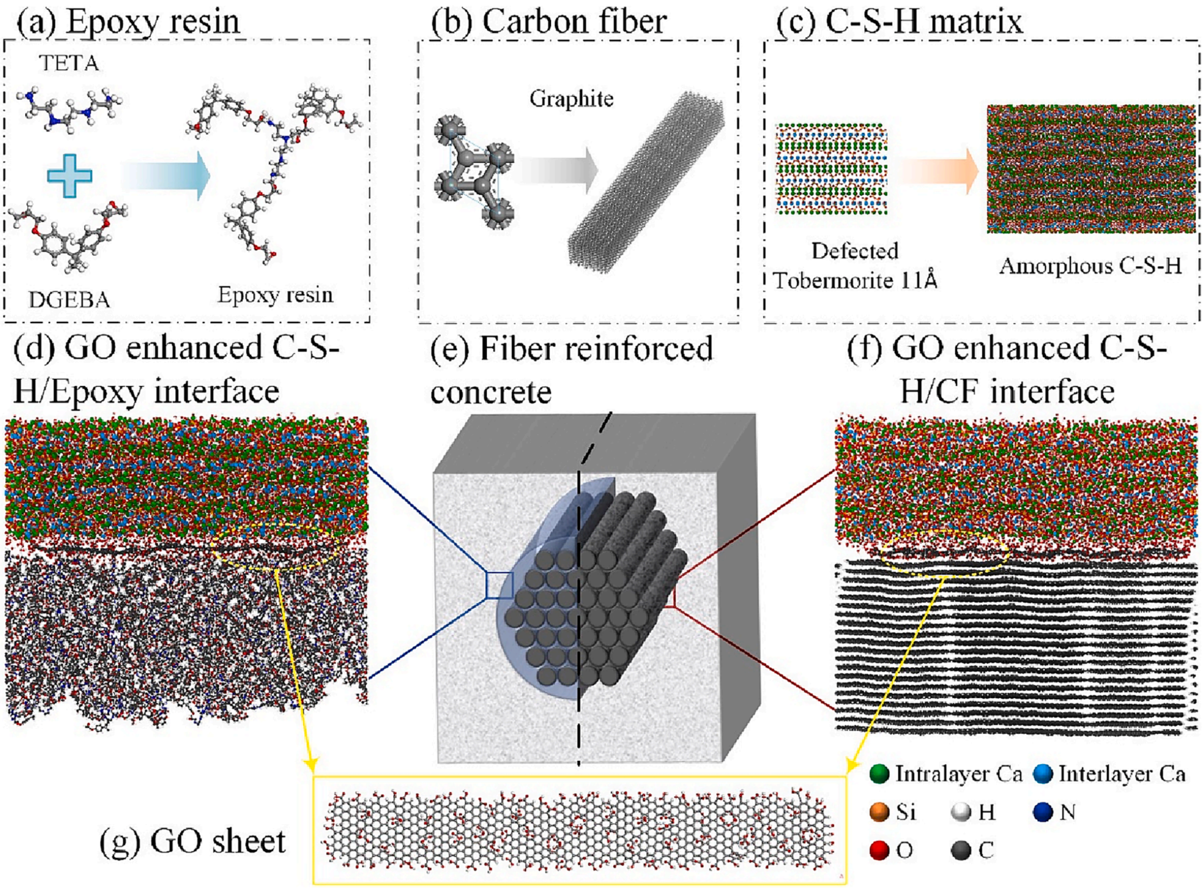

Fig. 1. Construction of molecular models. (a) Schematic illustration of the atomic structure of epoxy resin. (b) Unit cell and super cell of graphite. (c) Construction of amorphous C-S-H super cell. (d) Interface system of C-S-H and epoxy phases (with GO embedded). (e) Schematic illustration of carbon fiber reinforced cementitious composites. (f) Interface system of C-S-H and carbon fiber phases (with GO embedded). (g) Graphene oxide sheet with carboxyl functional groups.

enhance the cracking resistance of concrete [25–27]. The diameter of carbon fibers differs by several orders of magnitude from the geometric size of nano-additives, which allows them to improve the local morphology in concrete at the micro and nano -scales, respectively. And this synergistic effect can better improve the mechanical performance of the whole concrete sample [28,29]. By efficiently helping the ITZ between fibers and matrix to form denser and more homogenized structures, addition of 0.04 % graphene oxide (GO) by mass can increase the ITZ's fracture toughness from 0.994 MPa•m$^{1/2}$ to 1.241 MPa•m$^{1/2}$ [30]. Under the nano-filling effect and nucleation effect of GO, the originally disordered hydration products grow densely and aggregate into a regular polyhedron crystal structure, which greatly reduces the pore size of ITZ between the fiber and the matrix, and reduces the penetration depth of chloride ions in fiber-reinforced concrete [31,32]. Additionally, when the nano-additives can form more chemical bonds with the fiber surface, they can also effectively increase the frictional resistance between the fiber and the matrix to resist the fiber pullout during the cracking process [33]. Furthermore, nano-SiO_2 incorporation promotes geopolymerization, generating more amorphous gels, reducing porosity and optimizing microstructure, consequently improving the uniaxial compressive strength and durability of geopolymer recycled aggregate concrete [34]. Nano-SiO_2 grafted fibers have shown significant enhancement in the mechanical and fatigue properties of fiber-reinforced concrete. In rice straw fiber-reinforced concrete, the single-fiber pullout bonding strength was increased by 84.6 %, and the four-point flexural fatigue life was increased by four times [35]. This improvement can be attributed to nano-SiO_2's ability to decrease the presence of calcium hydroxide at the fiber–matrix interface and facilitate the formation of C-S-H gel, thereby densifying the structure of ITZ and mitigating the weak links [36].Under the synergistic effect of multiple additives at different scales, fly ash-CaCO3 whisker-steel fiber-reinforced concrete was able to increase the initial fracture toughness from 0.2 MPa•m$^{1/2}$ to 1.153 MPa•m$^{1/2}$ [37]. In addition to the enhancement of mechanical properties, nano-additives such as GO and multi-walled carbon nanotubes (MWCNTs) can enable the complete self-healing closure of micro-cracks through hydrogen bonding networks [38], or can also significantly reduce the electrical resistivity of concrete materials [39]. The application of GO in FRC is still in its infancy at present, and considering its complex mechanism, further study is needed to fully comprehend its reinforcing effect [25], particularly improvement of GO on the interfacial mechanical behavior at the molecular level.

The mechanical properties of cementitious composites at the nano-scale remain challenging to measure experimentally. Thus, many researchers turned to simulations to obtain mechanical responses of cementitious materials at the micro- or even nano-scale. This approach helps in understanding the role played by different phases at the micro or nano-scale. Fu et al. [40] utilized density functional theory and molecular dynamics to determine the elastic modulus of calcium hydroxide crystals and $(CaO)_{1.67}(SiO2)(H2O)_{1.75}$ [41]. Subsequent nano-indentation finite element simulations based on the elastic parameters obtained using the Mori-Tanaka and Self-Consistent homogenization methods revealed average C-S-H modulus of 18.11 GPa and 31.45 GPa for LD and HD C-S-H, respectively. These values were found to be comparable to the results from nanoindentation experiments conducted by Constantinides et al. [42], which reported values of 22.3 GPa and 33.5 GPa. Bauchy et al. [43,44] proposed a methodology that enables the calculation of fracture toughness and critical energy release rate of

C-S-H at the atomic scale through molecular dynamics simulations. This approach provides insights into the fracture properties of both brittle and ductile systems. Yang et al. [45] utilized molecular dynamics, homogenization theory, and effective medium theory to predict the thermal conductivity of nanomaterial-reinforced cementitious composites. Although the interaction between matrix and nanomaterials inhibits low frequency phonons, the large specific surface area of graphene and GO improves interfacial heat transfer, particularly due to the functional groups on the nanomaterials that improve the heat transfer efficiency at the nanomaterial–cement interfaces. Through molecular dynamics simulations, Zhou et al. [46] demonstrated that C-S-H gels tend to nucleate and grow on the surface of GO, forming high-strength Ca-O and Si-O bonds at the interface, thereby improving the mechanical properties and durability of cementitious matrix. Bahraq et al. [47] simulated the cement-epoxy interface and found that the introduction of graphene can effectively mitigates the diffusion of moisture and chloride ions. Under non-dry condition, the interaction between the epoxy and C–S–H is primarily driven by van der Waals forces. Despite the considerable body of literature exploring C-S-H and nano-additives at the nanoscale, there is limited research on the mechanical properties, particularly the nanoscale fracture properties of ITZ containing fibers and nano-additives. The impact of GO on the interfacial bonding behavior between carbon fiber and the cement matrix remains to be thoroughly addressed.

The primary objective of this paper is to investigate the mechanical reinforcement mechanism of GO in carbon fiber reinforced concrete. As one of the most vulnerable part in concrete, the interface between carbon fibers and C-S-H is the main target of this study. Considering that the carbon fibers incorporated into concrete can be either sized or un-sized, two molecular dynamics models were established, one for the interface between C-S-H and the sizing agent on the surface of the carbon fibers, and the other for the interface between C-S-H and the exposed carbon fibers in direct contact. Subsequently, the uniaxial tensile and fiber pullout damage modes of these two interface models was investigated, both with and without GO enhancement, to simulate the fiber interface debonding and pullout behavior during the damage process of the concrete structure. The mechanical responses during the damage process, such as damage strength and energy release rate, are the key characteristics we focus on. At the molecular level, the toughening mechanism of GO on the interface between carbon fibers and cement matrix is illustrated by analyzing the atomic configurations and interatomic interactions. This study contributes to a better understanding of the role of nano-additives and fibers in enhancing the mechanical properties of concrete, guiding researchers towards designing higher performance concrete materials from the nanoscale.

2. Computational methods

2.1. Model construction

In this paper, the interfaces between carbon fiber and cement matrix, which is the weak part in carbon fiber reinforced concrete, needs to be focused on. To simulate the mechanical behavior of its interface at the molecular scale, two all-atom models, the C-S-H/Epoxy and C-S-H/CF interfacial systems, were constructed. The former interface is used to simulate the interface formed between the cement matrix and the sizing agent on the fiber surface. Fig. 1 is a brief diagram of the main two interface model constructed in this research. Epoxy is a commonly used sizing agent in fiber production, and the most widely used diglycidyl ether bisphenol A (DGEBA) [48,49] was chosen as the epoxy phase in this paper. As shown in Fig. 1 (a), multiple epoxy molecules are cross-linked into a macromolecule by triethylenetetramine (TETA) [50,51]. The C-S-H/CF interface system is used to simulate the interface between C-S-H matrix and carbon fibers that are unsized or treated with acidic and alkaline solvents. Since the density of graphite is similar to that of commercial carbon fibers [52–54], about 1.78 g/cm^3, the atomic structure of graphite is used in this paper as an idealized model for carbon fibers (ignoring elements other than carbon in carbon fibers). Graphite unit cell ($a = b = 2.456$ Å, $c = 6.696$ Å; $\alpha = \beta = 90^\circ$, $\gamma = 120^\circ$) was extended to obtain a supercell representing the carbon fiber phase, as shown in Fig. 1 (b). The crystal structure of Tobermorite 11 Å [55], $a/2 = 5.58$ Å, $b = 7.39$ Å, $c/2 = 11.389$ Å; $\alpha = \beta = \gamma = 90^\circ$, is widely adopted as a C-S-H precursor atomic structure. To comply with the results of nuclear magnetic resonance (NMR) experiments [56], the C/S ratio should be adjusted to a value between 1.2 and 2.3 [57]. In this paper, a python script was used to randomly delete electrically neutral SiO_2 groups from infinite dreierketten chains in Tobermorite crystals, to achieve a C/S value near 1.7. Water adsorption simulations were then performed by Grand Canonical Monte Carlo (GCMC) simulation according to the method described by Pellenq et al [58,59] to fill the voids of the defective crystals with water molecules. Finally, reactive simulation at temperatures ranging from 300 K to 500 K was used to produce the amorphous C-S-H atomic structure illustrated in Fig. 1 (c). For more details of GCMC and reactive simulations, please refer to our previous work [60]. The two interfacial systems were finally obtained, C-S-H/Epoxy and C-S-H/CF, as shown in Fig. 1 (d) and (f), which represent the interfaces of sized and unsized carbon fibers in contact with the cement matrix, respectively. In order to enhance the mechanical properties of the fiber/matrix interface, graphene oxide sheets were added into the interfacial system. Fig. 1 (g) shows a sheet of graphene oxide with 20 % oxidation rate, which is obtained by unit cell expansion with $a = 2.46$ Å, $b = 4.26$ Å, $c = 3.4$ Å; $\alpha = \beta = \gamma = 90^\circ$. The carboxylic functional groups are randomly distributed around the edges as well as in the interior of the graphene sheet.

2.2. Force field

After GCMC water adsorption simulation, the reaction between SiO_4 chains and water molecules was carried out under reactive force field (ReaxFF) [61]. The water molecules in the interlayer and defective pores dissociate to produce OH^- and an H^+ ion pairs. The OH^- groups will coordinate with the interlayer Ca^{2+} ions, while the remaining H^+ atoms bind to the unbridged oxygen atoms of the SiO4 tetrahedra, then form Si-OH and Ca-OH groups. After 300 K ~ 500 K heating and 500 K ~ 300 K annealing simulations, the force field for C-S-H was switched to ClayFF [62,63], a force field specifically designed to characterize the structure of clays and minerals. The simple oxides, hydroxides, and oxyhydroxides systems are well simulated under the parameters of ClayFF [64]. It has been reported that ClayFF performs well in the structure prediction and bond strength simulation of silica mineral systems [40,65], Except for O-H bonds, ClayFF describes the interactions between elements (e.g., Ca, Si, and O) in the system by Lennard-Jones (12–6) potential, which greatly enhances the compatibility of the ClayFF force field. Therefore, in this paper, the ClayFF force field is adopted to describe the atomic interactions of C-S-H phases in complex interfacial systems. Also for compatibility reasons, consistent-valence force field (CVFF) [66] is used to describe the interatomic interactions of GO, CF and Epoxy phases in the interfacial system. The CVFF can not only simulate the thermal and mechanical properties of the organic systems designed in this paper [67–69], but also be well compatible with inorganic systems such as silicates [70,71]. The interatomic L-J interactions between the C-S-H phase and the GO, CF, Epoxy phases are combined using geometric rules (Lorentz-Berthelot).

2.3. Loading process

All molecular dynamics simulations in this paper were performed by the Large-scale Atomic/Molecular Massively Parallel Simulator (LAMMPS) [72], the Open Visualization Tool (OVITO) [73] and Visual Molecular Dynamics (VMD) [74] were used to render some of the atomic structure pictures. In this paper, the C-S-H and carbon fiber interfacial system is simulated under two loading patterns: uniaxial tension and

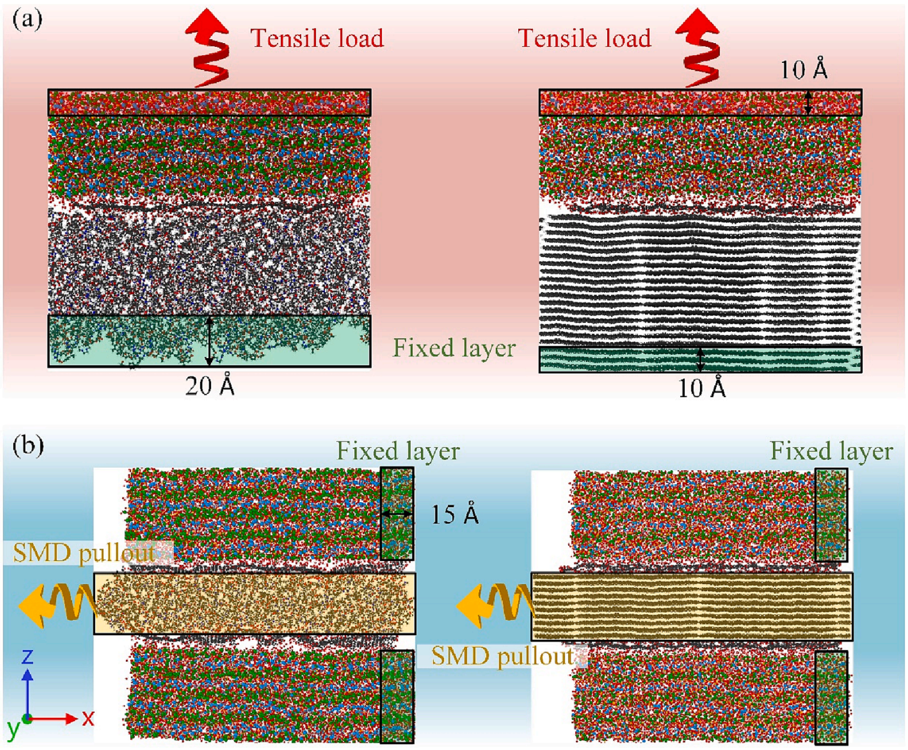

Fig. 2. Schematic illustration of the (a) uniaxial tensile process and (b) carbon fiber pullout process.

fiber pullout. Energy minimization of the interfacial system is required before the mechanical behavior simulation, and the minimization process is performed using a conjugate gradient algorithm to obtain a reasonable structure with the lowest energy. The system was then transferred to the NPT ensemble for equilibrium simulations for 2 ns, with the time step set as 1 fs, and the temperature was controlled by a Nose Hoover thermostat. As shown in Fig. 2 (a), an atomic layer of 10 Å thickness at the top of the simulation box in the Z-direction of the C-S-H/(GO)/Epoxy and C-S-H/(GO)/CF interfacial systems were set up as the loading layer during the uniaxial tensile simulation. A constant velocity along the positive direction of the Z-axis was applied at a strain increment of 10^{-7} per femtosecond, with the time step set as 1 fs. Correspondingly, the atomic layer at the bottom of the system needs to be immobilized. The thickness of the fixed atomic layer of epoxy phase is increased to 20 Å due to its irregular surface. Fig. 2 (b) shows the schematic diagram of the loading of carbon fiber pullout. Unlike the tensile process, the fiber pullout load is no longer applied by a constant velocity, but is instead by steered molecular dynamics (SMD) method [75], which allows the entire fiber to be pulled out from the interface. Standard SMD simulations can be performed by applying a spring potential constraint to manipulate specified molecules along prescribed paths in the configuration space. In SMD simulations of fiber pullout, a spring constant of 0.005 kcal/ (mol•Å^2) is applied to the CF or epoxy fiber clusters to pull it out of the interface at a constant velocity of 10^{-5} Å per femtosecond, and the time step was set as 1 fs. The force, energy and displacement information of the fiber pullout during the SMD simulation were used to analyze the mechanical behavior of the interfacial systems. In both uniaxial tensile and fiber pullout simulations, the boundary at loading direction is set to a non-periodic boundary condition to avoid cross-boundary atomic interactions. All the loading process simulations are carried out under the NVT ensemble to monitor the motion information of the atoms of the interface systems.

2.4. *Calculation of fracture properties*

At the nanoscale, fracture of materials is reflected by the breakdown of bonding or non-bonding interactions between atoms, resulting in the formation of pores and cracks. However, this process must be fundamentally distinct from continuum mechanics due to the structures and interactions of atoms. The energy release rate (G) [43] therefore can be used to describe the ability of interfacial systems at the atomic level to resist cracking.

$$\mathrm{W} = \frac{1}{2}\int_0^a p(x,0)\overline{u}Tdx \tag{1}$$

Here the W is the work done to extend the crack, the $p(x,0)$ is the crack normal stress distribution in the corresponding crack-free body. $\overline{u}$ is the total opening displacement of crack at position x, and T represents the thickness (Y-axis direction) of the simulated system. The energy release rate of the crack propagation can be expressed by the following Eq. (2),

$$\mathrm{G} = \frac{dW}{dA} = \frac{1}{2}\int_0^a p(x,0)\frac{d\overline{u}}{dA}Tdx \tag{2}$$

where A is the area of the corresponding crack. In this paper the crack area is determined by the projection of the free volume on the horizontal plane, using 1.8 times van der Waals radius as the full width at half maximum of Gaussian function [76]. The above equations are derived based on the traditional linear elastic fracture mechanics, and in order to exclude the influence of the plastic region on the estimated energy release rate, the equivalent crack area A_{eff} needs to be redetermined,

$$A_{eff} = A - \frac{L_y r_{pl}}{2} \tag{3}$$

where the phase subtracted by the area A is the area of the plastic zone at the crack tip, calculated by the Dugdale-Barenblatt method. The length of plastic region r_{pl} can be calculated by Eq. (4) [77]:

$$r_{pl} = \frac{a}{2}\left(\sec\left(\frac{\pi\sigma}{2\sigma_{pl}}\right)\right) \tag{4}$$

in which σ_{pl} represents the plastic yield stress,a is the initial crack length.

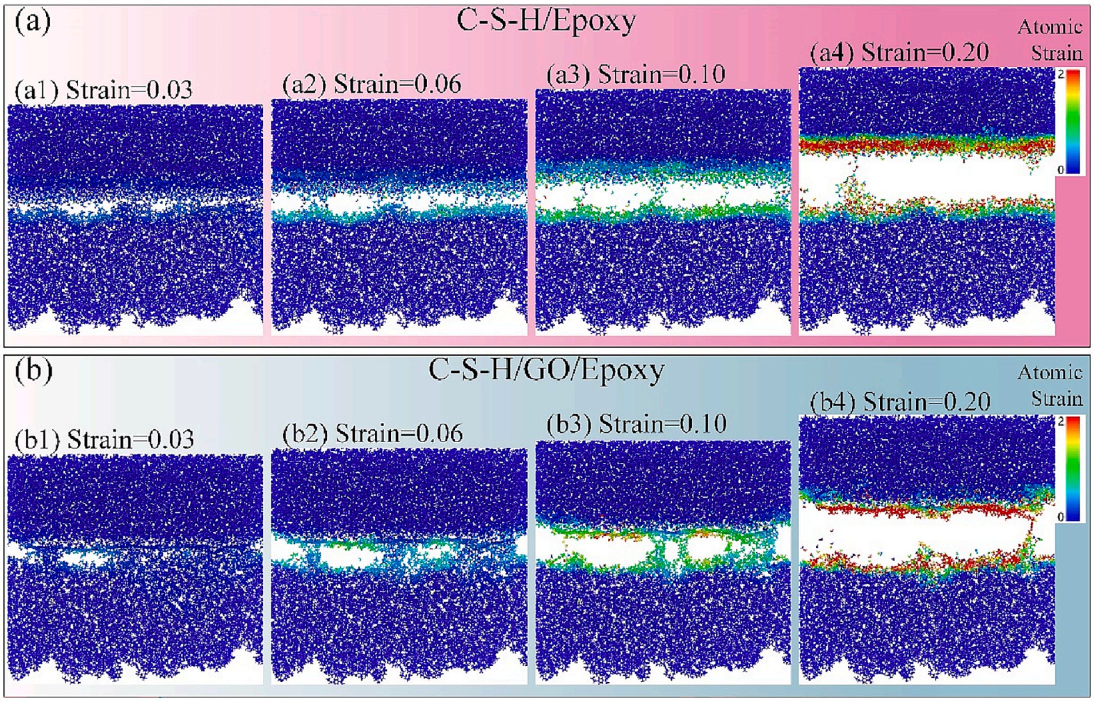

Fig. 3. Atomic strain of (a) C-S-H/Epoxy and (b) C-S-H/GO/Epoxy interface system under different tensile strains.

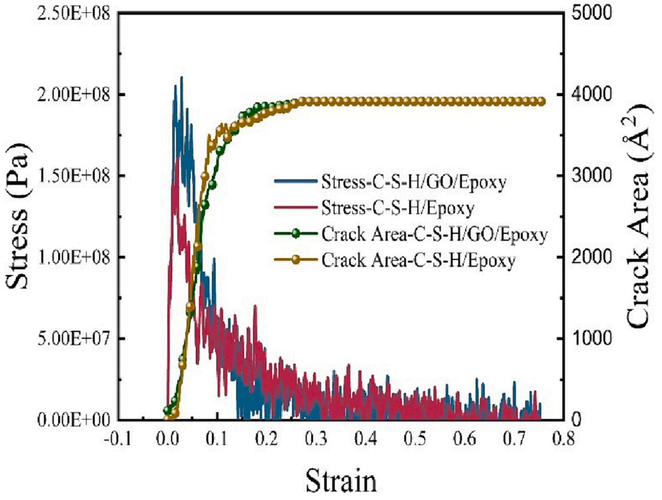

Fig. 4. Stress and crack area curves with strain.

For the opening mode (Mode-I), the relationship between critical energy release rate G_C and fracture toughness K_{IC} can be expressed by Eq. (5),

$$G_C = \frac{K_{IC}^2}{E'}, E' = \begin{cases} E, Planestress \\ \frac{E}{1-\nu^2}, Planestrain \end{cases} \tag{5}$$

where E' is related to Young's modulus E and Poisson's ratio ν. Here the plane strain case is applicable to our current study.

3. Results and discussion

Fiber-reinforced concrete performs better than ordinary concrete under flexural and tensile loading, which is primarily due to the prevention, delay, and deflection of microcracks in concrete by fiber bridging and fiber pullout. Therefore, uniaxial tensile and fiber pullout can be regarded as the two most important and typical failure processes of fiber-cement interface in fiber-reinforced concrete.

3.1. Interfacial performance of C-S-H/Epoxy composites

The atomic strain of the C-S-H/Epoxy and C-S-H/GO/Epoxy interfacial systems at tensile strains ranging from 0.03 to 0.20 are shown in Fig. 3 (a) and (b), respectively. Comparing the atomic strain at strain = 0.03 (a1 and b1), the system's configuration with GO incorporated in the interface shows smaller crack pores than the system without GO. It indicates that the addition of GO sheets improved the bonding between C-S-H and epoxy phase. At this strain, both interfaces reached the peak stress (see Fig. 4), and the maximum stress of the C-S-H/GO/Epoxy interfacial system (0.185 GPa) is 29.37 % higher than that of the C-S-H/Epoxy system (0.143 GPa). When the strain was increased to 0.1, the deformation difference between the two interfacial systems becomes more obvious, the cracks in Fig. 3 (a3) extended to almost the whole cross-section, and only a few water molecules were maintaining the hydrogen bonding holding the upper and lower surfaces together. In contrast, the interface in Fig. 3 (b3) has many epoxy molecules adhering to the GO sheet, and the right edge of the GO sheet even was twisted away from the C-S-H surface due to the interaction with epoxy atoms. The crack tip was significantly blunted and the crack extension was hindered by the bonding of epoxy molecules to GO and the bending deformation of GO itself. Similar phenomenon was observed by Hou et al. [78], in their study, it was mentioned that epoxy adhered to the GO sheet exhibits better resistance to pulling forces than that adhered directly to the CSH surface. This phenomenon is also supported by the crack area curve in Fig. 4, where the crack area of the C-S-H/Epoxy system is significantly larger than that of the C-S-H/GO/Epoxy interfacial system at strain = 0.1.

Fig. 5 (a) shows the curves of hydrogen bonds with strain in the C-S-H/Epoxy and C-S-H/GO/Epoxy systems. Before loading, the overall number of hydrogen bonds in the C-S-H/Epoxy system is larger than that in the C-S-H/GO/Epoxy system. This is because the number of water atoms within the interface in the C-S-H/GO/Epoxy system is less than that in the C-S-H/Epoxy. To facilitate comparison of energy changes between the C-S-H/GO/Epoxy and C-S-H/epoxy systems, the total number of this two systems are equal. Consequently, the total number of

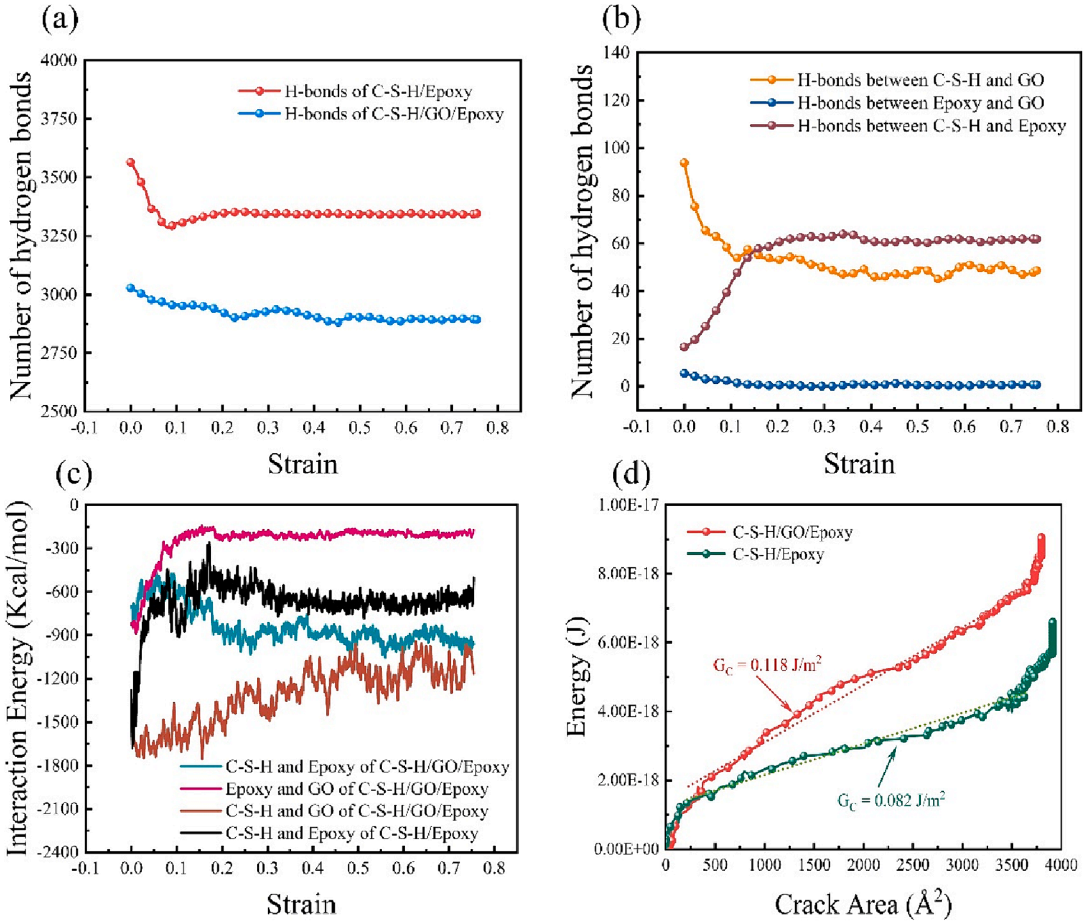

Fig. 5. (a) Variation of number of hydrogen bonds with tensile strain, (b) number of hydrogen bonds between three phases, (c) interaction energy between different components, (d) energy-crack area curve of C-S-H/(GO)/Epoxy interface systems.

water atoms removed from the C-S-H/GO/Epoxy system is equal to the total number of atoms in the embedded GO. As the strain increases to 0.1, the number of hydrogen bonds in the C-S-H/Epoxy system shows a drastic drop of 7.69 % to a global minimum point. In contrast, the number of hydrogen bonds in the C-S-H/GO/Epoxy system does not decrease to the first local minimum until strain = 0.22, with a decrease of 4.06 %. This demonstrates that compared to the C-S-H/Epoxy system, the hydrogen bonding in the C-S-H/GO/Epoxy system is less sensitive to strain. To further understand the specific distribution of hydrogen bonds among the three phases of C-S-H, GO, and epoxy, the variation of hydrogen bonds formed between three phases in the C-S-H/GO/Epoxy system can be seen in Fig. 5 (b). It's worth mentioning that during the statistical procedure, all water molecules in the interfacial gap were considered as the C-S-H phase. The amount of hydrogen bonds between the epoxy and GO phases stays at a low level, but also decreases slowly with the increase of strain, suggesting that the contribution of hydrogen bonding to the interfacial bonding between Epoxy and GO is very small. With a sharp drop in the number of hydrogen bonds between C-S-H and GO and a sharp increase between C-S-H and epoxy in the range of strain from 0 to 0.2, the number of hydrogen bonds between C-S-H and GO exhibit the opposite tendency to that between C-S-H and epoxy. The GO sheet divides the water molecules in the interfacial gap into two layers,

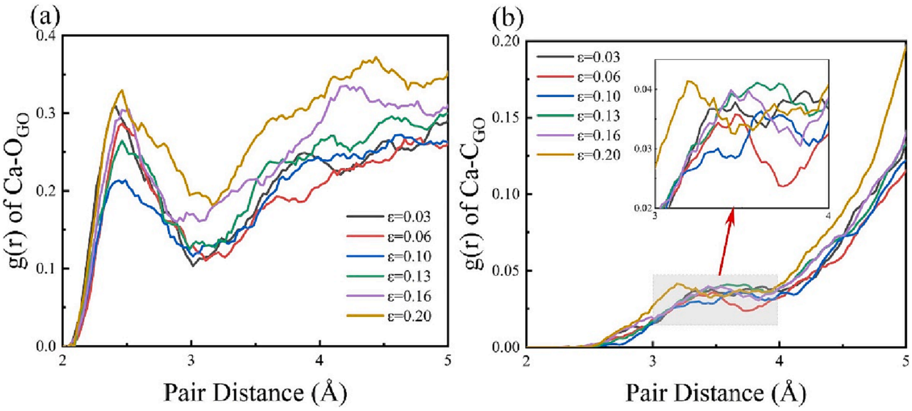

Fig. 6. Radial distribution function of (a) Ca-O_{Epoxy} pair, (b) Ca-C_{Epoxy} pair, (c) Ca-O_{GO} pair, and (d) Ca -C_{GO} pair in C-S-H/GO/Epoxy system.

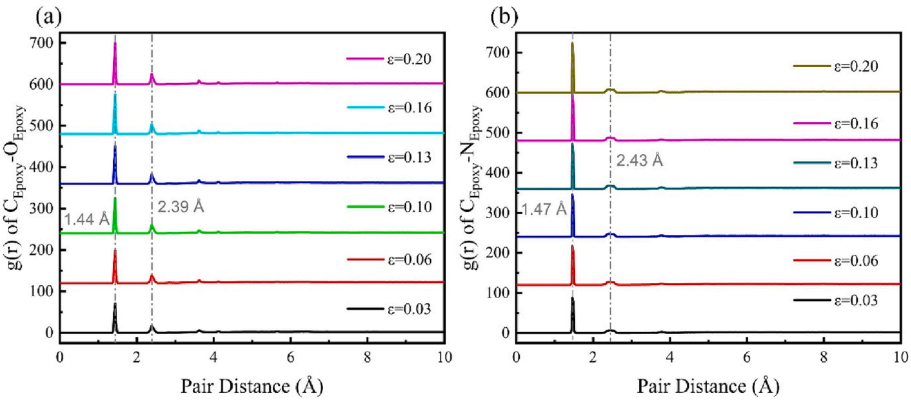

Fig. 7. Radial distribution function of (a) C_{Epoxy}-O_{Epoxy} pair and (b) C_{Epoxy} -N_{Epoxy} pair in the C-S-H/GO/Epoxy interface system.

and the water molecules closer to the epoxy surface gradually detach from the GO surface during the tensile process, and form hydrogen bonds with oxygen-containing groups in the epoxy.

By tracking the energy of the interfacial system during the stretching process, the intermolecular interaction energies between the phases in the interfacial system were obtained, as shown in Fig. 5 (c). For the C-S-H/Epoxy system, the interaction energy between the C-S-H and epoxy phases climbs to a local maximum value at strain = 0.1, which coincides with the trend of the hydrogen bonds in the system, and then reaches a global maximum value near strain of 0.2. The interaction energy between GO and epoxy phases in the C-S-H/GO/Epoxy system exhibits the same trend as that between C-S-H and epoxy in the C-S-H/Epoxy system. The interaction energy between C-S-H and epoxy in the C-S-H/GO/Epoxy system increases and then decreases with the strain, which is due to the detachment of water molecules mentioned in the hydrogen bonds analysis. Similarly, the interaction energy between C-S-H and GO increases as the GO sheet moves away from the gap water molecules. This series of energy curves suggests that embedding of GO sheet shifts the interfacial debonding from the C-S-H-epoxy phases to the GO-epoxy phases, which apparently have stronger interfacial bonding strength. The critical energy release rate G_C for tensile fracture of the whole system can be obtained from the energy-crack area curves, see Fig. 5 (d). The addition of GO leads a 43.90 % rise in the critical energy release rate of the C-S-H/Epoxy interface, from 0.082 J/m^2 to 0.118 J/m^2.

To clarify the contribution of interatomic interactions at interfaces to the resistance to fracture damage, the radial distribution function (RDF) of pairs of atoms between different phases in the system were investigated. The RDF reflects the probability of a class of atom pair appearing at a distance *r* from each other, and can be used to characterize the ordering of the atomic structure. The RDF curves of Ca and O_{GO} atoms in Fig. 6 (a) show that, the peak value gradually decreases when the strain increases from 0.03 to 0.1, with the position shifted from 2.4 Å to 2.5 Å. When the strain continues to increase to 0.13 or even 0.2, peak value begins to increase and even exceeds that of the 0.03 strain. Ca and C_{GO} atom pairs exhibit the same response (see Fig. 6 (b)). GO gradually moves away from the C-S-H phase under the bonding force with the epoxy surface at strains lower than 0.1. However, as the strain continues to increase, the interatomic interactions between GO and the epoxy phase become insufficient to withstand the tensile deformation and cracks. Finally, GO gradually reestablishes its close connection with the C-S-H phase. This suggests that calcium ions play the role of a link between C-S-H and GO, which is consistent with the findings of Luo et al. [79]. However, there is no significant spatial correlation can be observed between Ca and O_{Epoxy} or C_{Epoxy} atoms within the range of atomic distances less than 5 Å.

As shown in Fig. 7 (a) and (b), except for a slight change in the value of peaks, the positions of the peaks are not shifted in the RDFs of the C-O and C-N atom pairs in the Epoxy phase. This indicates that the strain is not well transferred to the epoxy phase, and most of the epoxy molecular chains are still in a tightly folded state. The RDFs between the O_{GO} atoms and the N_{Epoxy} or C_{Epoxy} atoms show a decrease of peak value and an increase of the corresponding pair distance from 0.03 to 0.16, (see Fig. 8 (a), (b)). O_{GO}-C_{Epoxy} pairs exhibit the greatest strain sensitivity, which points to their major contribution to the interfacial bonding between GO and epoxy to resist tensile cracking.

Similarly, the interatomic RDFs within the epoxy phase of the C-S-H/Epoxy interfacial system show insensitivity to strain, only Ca-O_{Epoxy} pair changes significantly with strain at strain < 0.06 (see Fig. 9). Overall, these results indicate that Ca-O_{Epoxy} interatomic interactions contribute to resisting deformation at low strains, but due to the stiffness mutation in the interface, the strain is not well transmitted to the epoxy phase. Instead, intra-interfacial hydrogen bonding is the main mechanism for

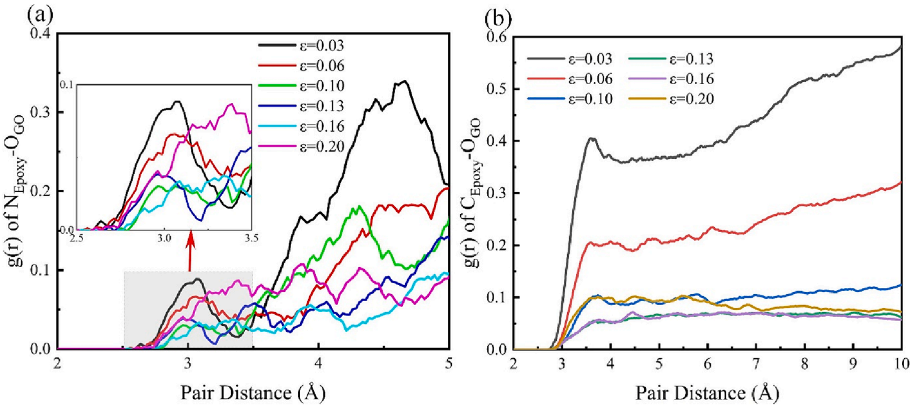

Fig. 8. Radial distribution function of (a) N_{Epoxy} - O_{GO} pair and (b) C_{Epoxy} - O_{GO} pair in the C-S-H/GO/Epoxy interface system.

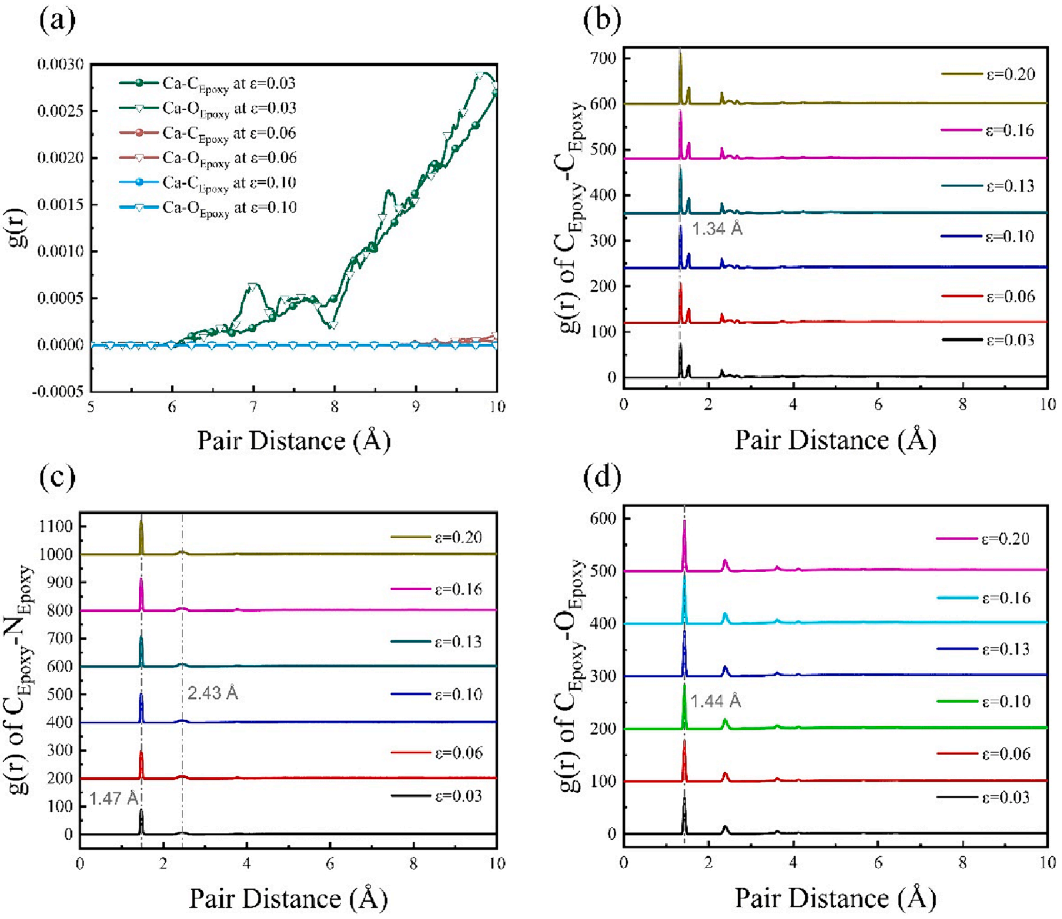

Fig. 9. Radial distribution function of (a) Ca-C$_{Epoxy}$ and Ca-O$_{Epoxy}$ pair, (b) C$_{Epoxy}$ -C$_{Epoxy}$ pair, (c) C$_{Epoxy}$ -N$_{Epoxy}$ pair, (d) C$_{Epoxy}$ -O$_{Epoxy}$ pair in the C-S-H/Epoxy interface system.

resistance to deformation at $0.06 < \text{strain} < 0.1$ (the number of hydrogen bonds is still strongly sensitive to strain). The disruption of the interaction between the C-S-H layer and the epoxy resin is pronounced as water molecules diffuse into the localized interfacial region. This phenomenon arises from the coordination of interfacial water with calcium ions, and subsequently forms hydrogen bonding network with oxygen-containing functional groups in the epoxy resin near the interface. Yu et al. [80] also pointed out that the absorption of the water in local interfacial region could impair the adhesion between cement and epoxy in the interface.

Atomic snapshots of fiber pullout simulations for the C-S-H/Epoxy interfacial system are shown in Fig. 10 (a1-a4). Epoxy fibers with an average thickness of 35 Å are embedded between two layers of C-S-H, and then pulled out of the C-S-H matrix along the horizontal left at a constant rate. At a pullout displacement of 100 Å, the end of the epoxy fiber shows a large deformation due to friction with the C-S-H phase. When the displacement is increased to 150 Å, the fiber has been completely pulled out of the interface, but the deformation of the epoxy fiber is still unrecovered, indicating that the interaction during the pullout process has caused irreversible plastic deformation on the fiber. There are more details can be observed in the pullout of the C-S-H/GO/Epoxy interfacial system demonstrated in Fig. 10 (b1-b4). Due to the molecular chains on the uneven epoxy surface, several local folds can be seen in the GO sheets embedded between the epoxy fibers and the C-S-H phase (see local magnification in Fig. 10 (b1)). When the displacement is increased to 50 Å, all the folds have been flattened by the friction unfolding through the pullout process, and a large number of epoxy molecules are left in the original folded positions on the GO sheets. Until the displacement increases to 150 Å, a significant number of epoxy molecular chains are adsorbed on the surface of both GO sheets, leading rough surfaces of epoxy fiber. Due to the substantial plastic deformation brought on by the strong bonding with the GO sheets, the epoxy fiber end is still not completely separated from the C-S-H matrix at 150 Å. It is worth mentioning that the fiber pullout simulation's final displacement is 180 Å, which allows fiber to be entirely drawn out of the interface.

Fig. 11 (a) records the force–displacement curves and crack area-displacement curves during fiber pullout. The interfacial system with GO embedded has an ultimate pullout displacement of 175 Å, which is higher than 155 Å of the C-S-H/Epoxy system. This indicates that the addition of GO increases the friction at the fiber pullout interface, absorbs more energy, thus leads to longer ductile deformation. In addition, the incorporation of GO increases the maximum pullout force by 40.94 %, from 1.27×10^{-8}N to 1.79×10^{-8}N. The crack area of the C-S-H/Epoxy system increases almost linearly during fiber pullout, which is consistent with the constant rate pullout set by SMD. On the other hand, the crack area curves of the C-S-H/GO/Epoxy system often show a stage of decreasing slope, which is related to the plastic deformation or even peeling from the surface of epoxy fiber. According to Fig. 11 (b), embedding GO indeed enhance the energy dissipated during the pullout process of epoxy fibers, with a 22.64 % increase in the critical energy release rate from 1.175 J/m^2 to 1.441 J/m^2. The contribution of the interfacial components to resisting deformation can be more clearly clarified through their interaction energies, see Fig. 11 (c). The interaction energy curves between the C-S-H phase and the epoxy phase in the two interfacial systems mostly overlap, indicating that the extra energy consumed by the C-S-H/GO/Epoxy system to resist the damage compared with that of the C-S-H/Epoxy system is almost entirely contributed by the interaction between the GO and epoxy phases.

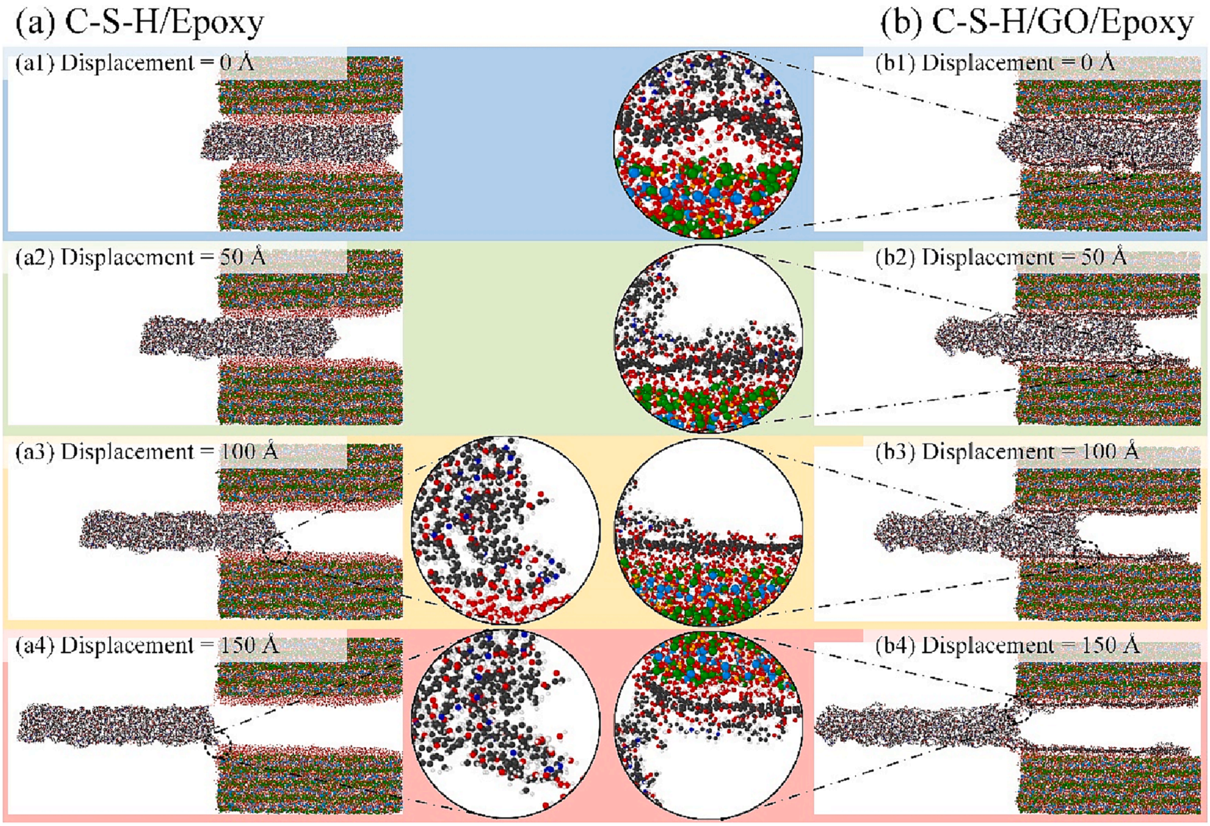

Fig. 10. Atomic snapshots of C-S-H/Epoxy (a1-a4) and C-S-H/GO/Epoxy (b1-b4) pullout simulation at different pullout displacement.

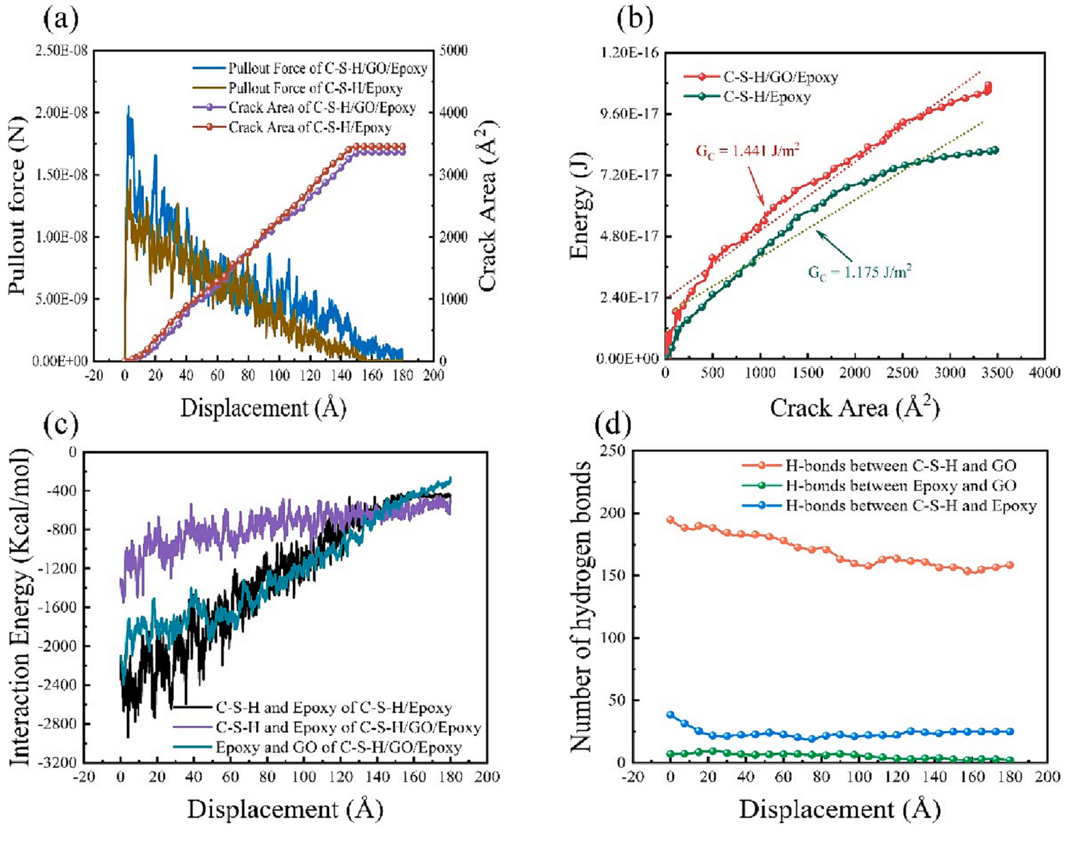

Fig. 11. (a) Force and crack area curves with pullout displacement. (b) Energy-crack area curve of C-S-H/(GO)/Epoxy pullout systems. (c) Interaction energy between different components in the pullout systems. (d) Variation of number of hydrogen bonds with pullout displacement of C-S-H/GO/Epoxy system.

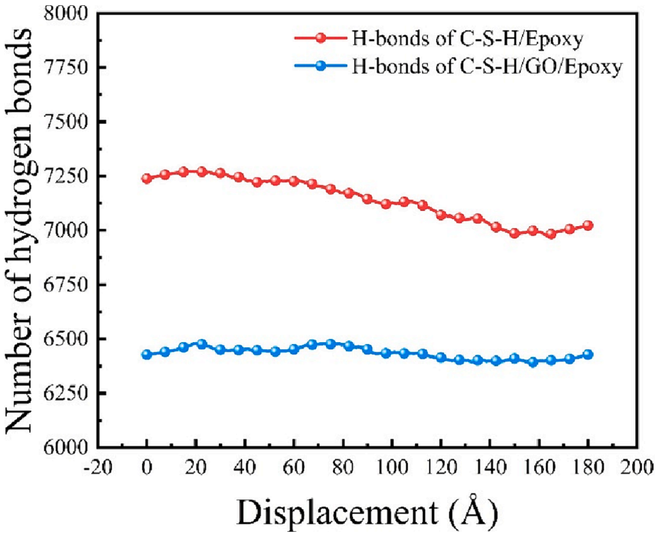

Fig. 12. Total number of hydrogen bonds with pullout displacement of C-S-H/(GO)/Epoxy systems.

Fig. 12 shows the overall hydrogen bonds number changes during fiber pullout for the C-S-H/Epoxy and C-S-H/GO/Epoxy systems. In the system without GO, the number of hydrogen bonds decreases as displacement increasing until the fiber completely pulled out (155 Å). This result confirms that the contribution of hydrogen bonding to the C-S-H/Epoxy interfacial system in resisting the fiber pulling out is consistent throughout the process. In contrast, the hydrogen bonding in the C-S-H/GO/Epoxy system is insensitive to the pullout displacement. It is further confirmed that hydrogen bonding is no longer the primary factor contributing to the pullout resistance in the C-S-H/GO/Epoxy system by the of hydrogen bonds curves between C-S-H, GO and epoxy, respectively, as shown in Fig. 11 (d).

3.2. *Interfacial performance of C-S-H/CF composites*

In this section, the mechanical response of the interfacial system of carbon fiber (CF) without sizing in direct contact with C-S-H will be investigated. The atomic strain of C-S-H/CF and C-S-H/GO/CF interfacial systems under uniaxial tensile loading are shown in Fig. 13 (a) and (b), respectively. At a low strain of 0.03, the strain is not uniformly distributed and some pores preferentially form continuous cracks and generate larger atomic strains. When the strain continues to increase to 0.1, the C-S-H/CF system has already developed a cross-section crack (the crack area curve in Fig. 14 (a) has reached the maximum value), which means that the interface has been completely destroyed. In the C-S-H/GO/CF system, however, many molecules are still connected to the upper and lower surfaces of the crack. The GO is tightly adsorbed on the CF surface due to van der Waals and π-π interactions with graphite molecules [81]. There is no warping or deformation of the GO edges observed as in the C-S-H/GO/Epoxy system. Therefore, the incorporation of GO sheets changes the interfacial debonding behavior from between C-S-H and CF to between C-S-H and GO. As can be seen in Fig. 13 (b4), the lower surface of C-S-H and the upper surface of GO in the C-S-H/GO/CF system have very large and concentrated atomic strains.

The maximum tensile stress of C-S-H/GO/CF is 0.172 GPa, which is 63.81 % higher than that of 0.105 GPa for the system without GO. Overall, the critical energy release rate G_C is increased by GO from 0.078 J/m^2 to 0.107 J/m^2, a 37.18 % increase (see Fig. 14 (b)). Since the CF surface does not contain any polar functional groups, the interfacial bonding of CF surface in direct contact with C-S-H is much lower than that of epoxy and C-S-H. However, a significant number of oxygen-containing groups on GO can raise the maximum stress of this interfacial bonding to a level that is comparable to that of the C-S-H/Epoxy interface. On the other hand, the adhesion between GO and CF is so stable that the system does not exhibit the similar failure behaviors of C-S-H/Epoxy interface, such as GO bending deformation and epoxy molecular exfoliation, which dissipate a lot of energy and passivate the tip of the crack. So the critical energy release rate of the interface between C-S-H and CF is lower than that of the interface between C-S-H and epoxy systems, regardless of whether there is GO enhancement.

The contribution of the interaction energy between C-S-H, GO and CF

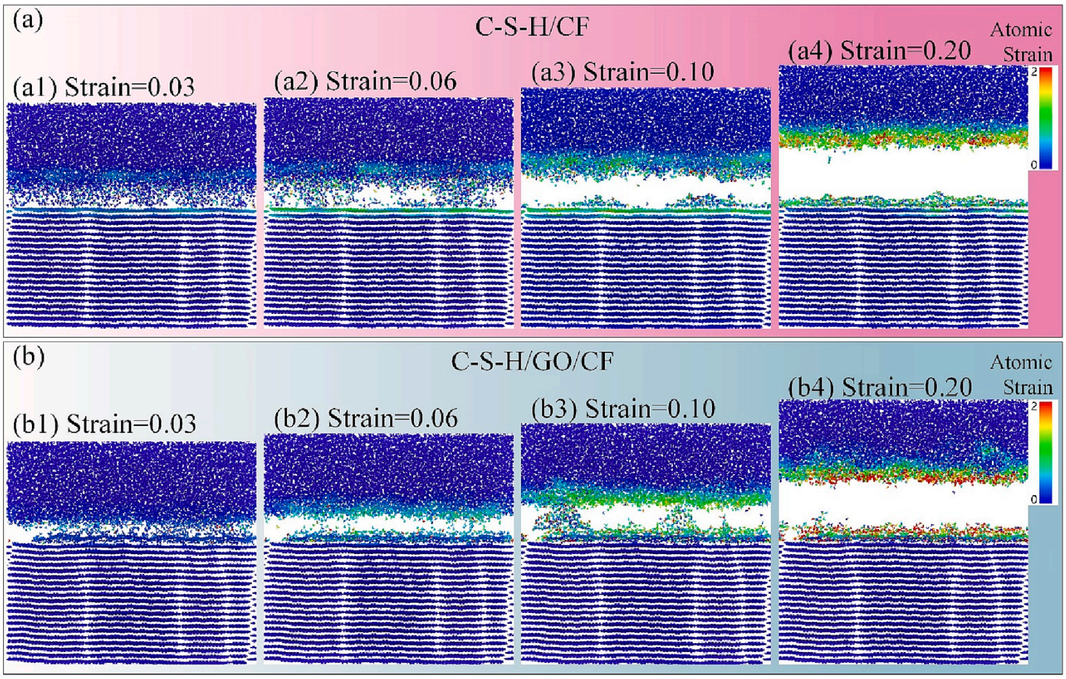

Fig. 13. Atomic strain of (a) C-S-H/CF and (b) C-S-H/GO/CF interface system under different tensile strain.

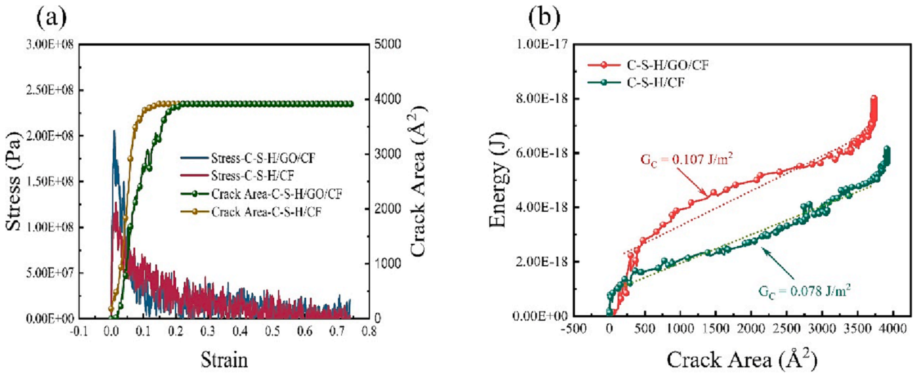

Fig. 14. (a) Stress and crack area curves with strain. (b) Energy-crack area curve of C-S-H/(GO)/CF interface systems.

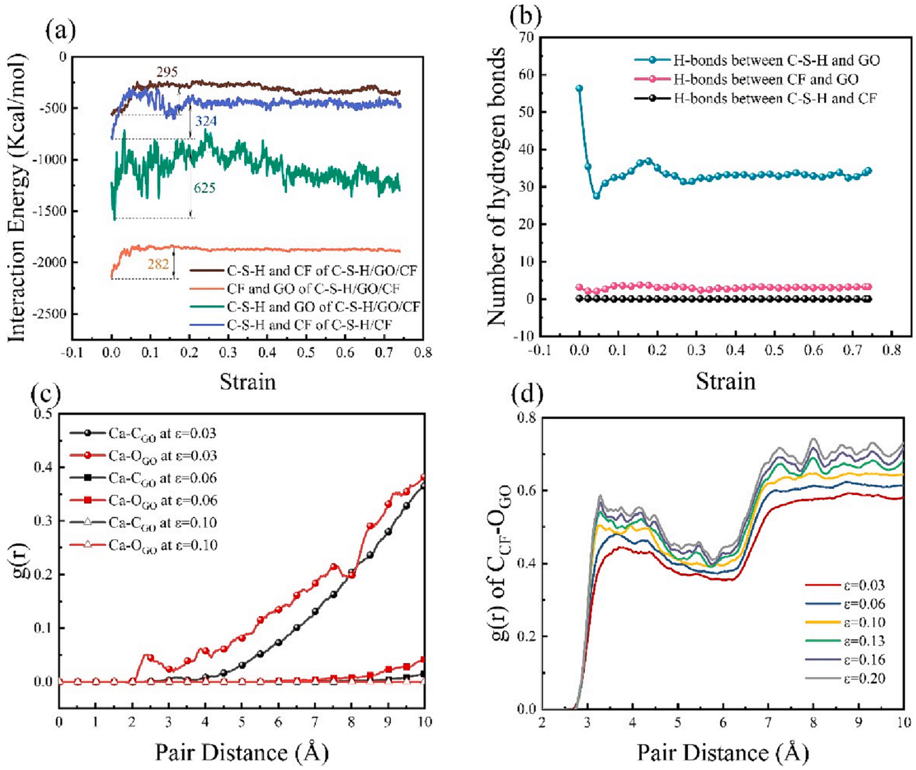

Fig. 15. (a) Interaction energy between different components in the interface systems. (b) Variation of number of hydrogen bonds with tensile strain of C-S-H/GO/CF system. (c) Radial distribution function of Ca-C_{GO} and Ca-O_{GO} pair. (d) Radial distribution function of C_{CF}-O_{GO} pair.

to resist tensile damage is shown in detail in Fig. 15 (a). In the C-S-H/CF system, there are only two phases, and the energy between them increases by about 324 Kcal/mol as the strain goes from 0 to 0.2. The interaction between the C-S-H phase and GO consumes its most energy at the C-S-H/GO/CF interface, increasing by 625 Kcal/mol. Then the next two are C-S-H and CF, GO and CF, increase by 295 Kcal/mol and 282 Kcal/mol, respectively. This is consistent with the conclusion made above that the embedding of GO changes the interface damage mode from the fragile C-S-H-CF interface to the stronger C-S-H-GO interface.

The number of hydrogen bonds in both interface systems in Fig. 16 (a) show a similar change trends to that of the C-S-H/Epoxy system in Fig. 5 (a). The number of hydrogen bonds decreases in an almost linear pattern to a minimum point with the beginning of tension. The difference with the C-S-H/Epoxy system is that the minimum position of the C-S-H/(GO)/CF system is advanced from around 0.1 to around 0.05, indicating a reduced interfacial yield strain between CF and C-S-H. Fig. 15 (b) details the distribution of the number of hydrogen bonds between C-S-H, GO, and CF. It is obvious that the hydrogen bonds are formed almost exclusively between C-S-H and GO, which have a large number of oxygen-containing functional groups. According to the RDF in Fig. 15 (c), at strain = 0.03, there is a significant spatial correlation between Ca and O_{GO} at a distance of 2.4 Å, while there is no spatial correlation between Ca and C atoms in GO. As the strain increases beyond 0.06, both Ca-O_{GO} and Ca-C_{GO} are no longer spatially correlated, indicating that the C-S-H matrix has separated from the GO surface at this strain. The RDFs of the C atoms in CF and the O atoms in GO are shown in Fig. 15 (d), The first peak of the RDF rises with strain and moves from 3.9 Å to 3.4 Å, the latter distance being close to the interlayer spacing of graphite. The abrupt change in peak position from strain = 0.06 to 0.10 suggests that the C-S-H matrix completely debonds from the GO surface during this strain interval. The crack surface then appears as a result, and the GO binds more tightly to the CF, with losing its interatomic interaction with the C-S-H.

The pullout the CF from the C-S-H matrix also was performed, to

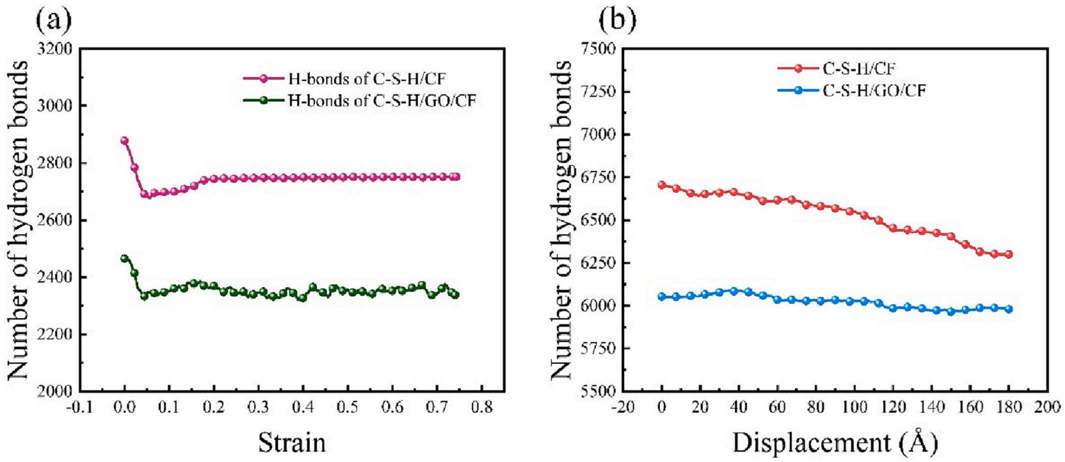

Fig. 16. Variation of number of hydrogen bonds with (a) tensile strain and (b) pullout displacement of C-S-H/(GO)/CF systems.

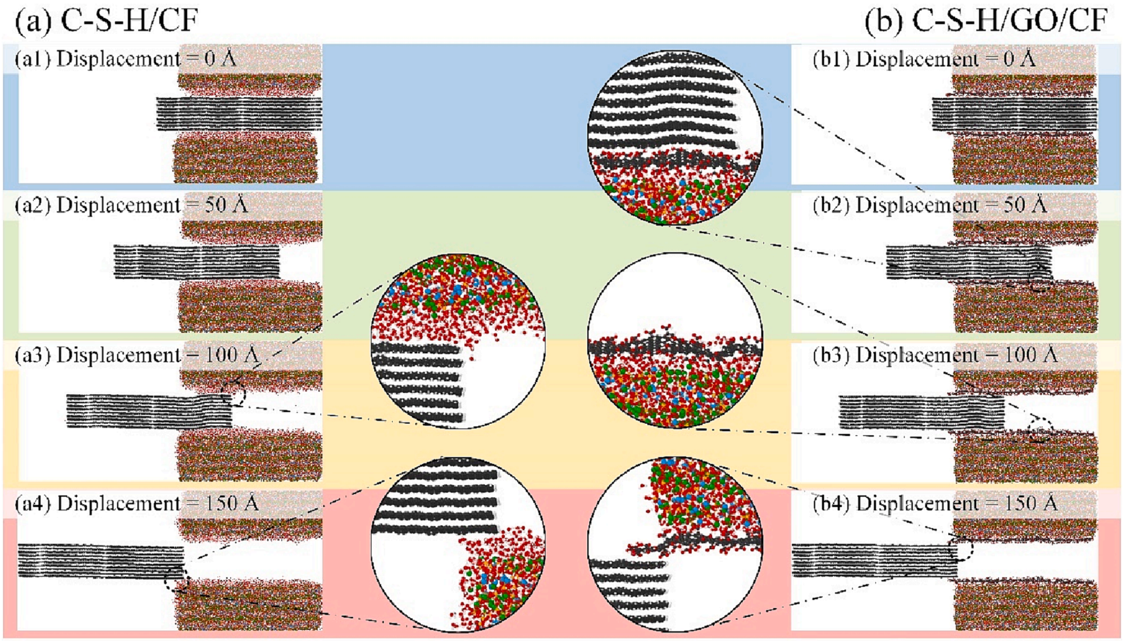

Fig. 17. Atomic snapshots of C-S-H/CF (a1-a4) and C-S-H/GO/CF (b1-b4) pullout simulation at different pullout displacement.

study the mechanical response of the C-S-H/(GO)/CF interfacial system. As observed in Fig. 17 (a1-a4), some water molecules are taken out from the center of the interface to the left side due to friction of CF. Due to the smooth surface of the CF, the migration of these water molecules acts as a "lubricant" in the pullout process. After embedding GO, the water molecules in the C-S-H/GO/CF interface are attracted by the more hydrophilic GO, as shown in Fig. 17 (b1-b4). It is worth noting that the GO inside the interface maintains no slip on the C-S-H surface rather than adhering to the CF surface as in the case of tensile simulation. This is because the surface of C-S-H is sufficiently rough, and the van der Waals force with GO as well as the coulombic force between Ca and O_{GO} are strong enough to resist the shear force inside the interface.

As shown in Fig. 18 (a), the crack extension rates of the C-S-H/GO/CF and C-S-H/CF systems are nearly identical for displacements less than 120 Å. The pullout force exhibits considerable oscillation due to the periodic repeating units in the CFs' structure along the loading direction. The embedding of GO increases the maximum pullout force of the C-S-H/CF interfacial system by 63.65 %, from 5.20×10^{-9}N to 8.51×10^{-9}N. As a result, the critical energy release rate increased from 0.685 J/m^2 to 0.977 J/m^2, an increase of 42.63 %, see Fig. 18 (b). The increment of interaction energy between CF and GO is about 1.8 times higher than that between CF and C-S-H, as shown in Fig. 18 (c), which suggests that the atomic interactions between CF/GO are the most dominant contribution to the resistance against interfacial pullout damage. Since CF do not have oxygen-containing functional groups, the hydrogen bonding in the system is concentrated between C-S-H and GO. The bonding between C-S-H and GO is relatively stable leading to the insensitivity of the hydrogen bonds to the pullout deformation, which can be seen from Fig. 18 (d).

3.3. *Implications for design fiber reinforced concrete*

Since there are fewer direct tensile experiments on micro-scale carbon fiber reinforced concrete, we also refer to indirect fracture toughness values obtained from flexural strength test in some of the studies. Generally we believe that these indirect tensile strength values are not equal to the direct uniaxial tensile strength values, and the scale of the specimen has a very strong influence on the strength values [82]. First, we compared molecular dynamics calculations with experimental results for pure C-S-H phases, as previously reported by other researchers,

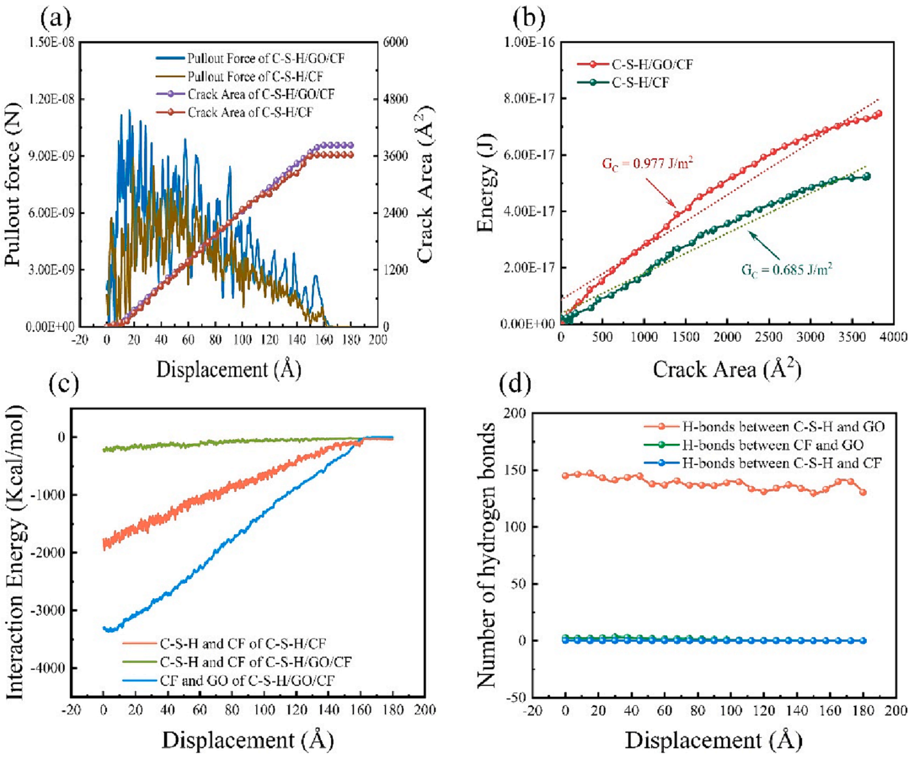

Fig. 18. (a) Force and crack area curves with pullout displacement, (b) Energy-crack area curve of C-S-H/(GO)/CF pullout systems. (c) Interaction energy between different components in the pullout systems. (d) Variation of number of hydrogen bonds with pullout displacement of C-S-H/GO/CF system.

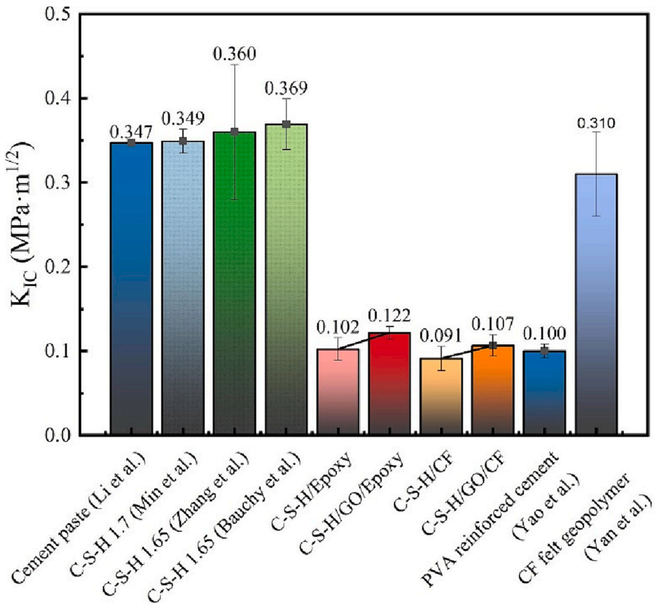

Fig. 19. Fracture toughness of C-S-H – fiber interface calculated in this paper and results of similar structures in literatures.

see Fig. 19. Li et al. [83] determined the fracture toughness of plain cement paste using the electrochemical impedance method and found it to be approximately 0.347 MPa/m^2. Molecular dynamics calculations, conducted with varying C/S ratios [43,44,84], yielded results ranging from 0.349 to 0.369 MPa/m^2. These calculated values are consistent with the experimental data, demonstrating good agreement between the molecular dynamics method and empirical observations. This paper focuses on the ITZ between the cement matrix and carbon fiber. The fracture toughness values presented in this study are approximately one-third of those found in pure C-S-H systems, primarily due to the introduction of a fragile interphase interface. Yao et al. [85] conducted bending experiments on polyvinyl alcohol fiber reinforced cement composites and reported a fracture toughness of 0.10 MPa/m^2. This result is in good agreement with the fracture toughness of the C-S-H/Epoxy and C-S-H/CF interface systems investigated in this paper. Yan et al. [86] conducted flexural experiments on carbon fiber felt reinforced geopolymer composites, reporting a fracture toughness of 0.31 MPa/m^2. Even after accounting for potential overestimations in the flexure experimental results, this value remains significantly higher than the fracture toughness of the C-S-H/Epoxy and C-S-H/CF interfacial systems investigated in this paper. This is due to the atomic structure established in this paper only focuses on the most fragile interfacial region in the FRC, and the system completely relies on the bond between the fiber and the matrix to resist fracture. While fracture events in the macroscopic specimen encompass not only the ITZ but also extend to the fracture within the matrix, the fibers, and the bridging of the fibers within microcracks. As a result, the overall fracture toughness of the specimen exceeds that of the localized pure ITZ structure.

As illustrated in Fig. 19, the ITZ formed between epoxy or CF and C-S-H exhibit lower fracture toughness than that of the matrix phase. Consequently, cracks tend to initiate in the interface region rather than within the matrix. The fracture toughness of the C-S-H/Epoxy interface increased from 0.102 MPa/m^2 to 0.122 MPa/m^2 with the addition of GO flakes, representing a 19.61 % improvement. Similarly, the fracture toughness of C-S-H/CF increased by 17.58 %, rising from 0.091 MPa/m^2 to 0.107 MPa/m^2. These results suggest that the introduction of GO does indeed have a significant toughening effect on the ITZ between carbon fiber and the cement matrix. It's worth noting that the epoxy phase within sized carbon fibers can create a more adhesive interface with C-S-H, characterized by higher fracture strength and toughness compared to unsized carbon fibers. This observation indicates that rougher fiber surfaces with more polar functional groups are better suited for reinforcing concrete, in contrast to smooth fiber surfaces lacking oxygen-containing functional groups. This finding aligns with experimental

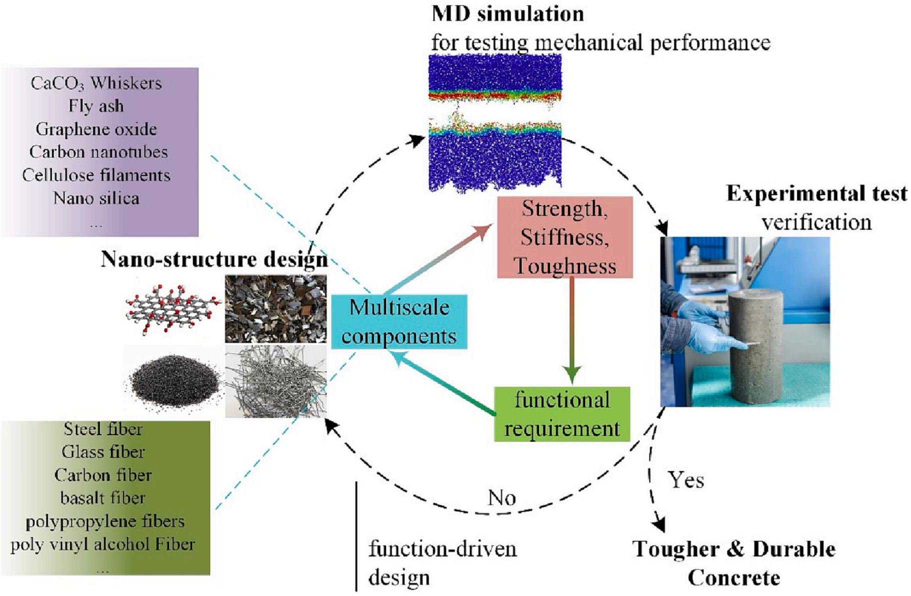

Fig. 20. The “bottom-up” design of high-performance concrete.

studies advocating for chemical surface modification of fibers prior to their incorporation into concrete [87]. Chemical grafting or deposition of GO in the form of a thin film on the surface of carbon fibers can achieve the desired effect of reinforcing ITZ, as proposed in the model presented in this paper. Researchers can try to immerse carbon fibers into cationic polyelectrolyte to obtain electropositive carbon fiber surfaces. The electrostatic interaction facilitates the layer-by-layer deposition of electronegative GO sheets and electropositive SiO_2 nanoparticles (amination modifying SiO_2: SiO_2–NH_2) onto the carbon fiber surfaces [88]. Fig. 20 outlines a function-driven “bottom-up” design method presented in this paper. When confronted with concrete structures requiring specific macroscopic performance attributes, researchers initially search for optimal microscopic phase combinations through nanoscale structural design. These phases may incorporate various additives commonly used in high-performance concretes, such as carbon fiber, steel fiber, polypropylene fiber, polyvinyl alcohol fiber, as well as a diverse range of nano-additives like GO, carbon nanotubes, and fly ash, etc. Subsequently, the designed nanostructures undergo MD simulations, providing a preliminary verification of the mechanical properties. This approach can significantly reduce testing costs at the early design stage, offering researchers greater design flexibility.

4. Conclusions

In this study, two atomic interfaces, C-S-H/Epoxy and C-S-H/CF, were established to characterize the interfaces between carbon fibers and cement matrix in fiber-reinforced concrete. Uniaxial tensile and fiber pullout process were simulated using molecular dynamics methods. The results demonstrate that the embedding of GO sheets strengthened the bonding between C-S-H and carbon fiber interfaces.

Specifically, in the case of epoxy sizing, GO increased the uniaxial tensile and fiber pullout strengths of the C-S-H/Epoxy interface by 29.37 % and 40.94 %, respectively, while the critical energy release rate of uniaxial tensile and fiber pullout increased by 43.90 % and 22.64 %, respectively. Similarly, when the C-S-H was in direct contact with carbon fibers without sizing agent, the uniaxial tensile and fiber pullout strengths increased by 63.81 % and 63.65 %, and the critical energy release rates increased by 37.18 % and 42.63 %, respectively. For the epoxy-coated fibers, the embedding of GO sheet shifted the interfacial debonding from between C-S-H and epoxy phase to between GO and epoxy phases. On the other hand, for the unsized carbon fibers, failure occurred between the C-S-H phase and GO. Overall, the enhancement effect of GO on the bond strength at the C-S-H/CF interface is more pronounced. The analysis of the RDF and hydrogen bonds shows that the interaction between Ca^{2+} ions and O atoms in the carboxyl group, as well as hydrogen bonding, play an important role in bonding GO and C-S-H phase and resisting the cracking. For the bonding between GO and epoxy or CF phases, the contribution of hydrogen bonding is almost negligible, and C-O and N-O atom pairs are more sensitive to strain compared to other pairs. By understanding the damage process of the fiber–matrix interface at nanoscale, researchers can utilize molecular design to screen specified concrete materials with complex structures and optimized properties in construction engineering field.

CRediT authorship contribution statement

Benzhi Min: Methodology, Software, Writing – original draft, Conceptualization. **Guoliang Chen:** Validation, Visualization, Writing – review & editing. **Yongyang Sun:** Formal analysis, Investigation. **Ke Li:** Conceptualization, Visualization. **Xi Chen:** Data curation, Software, Visualization. **Zhenqing Wang:** Project administration, Supervision, Writing – review & editing.

Declaration of competing interest

The authors declare that they have no known competing financial interests or personal relationships that could have appeared to influence the work reported in this paper.

Data availability

Data will be made available on request.

Acknowledgement

This work was supported by the National Natural Science Foundation of China with Grant NO. 11532013 and 11872157. The authors gratefully acknowledge computing support from National Supercomputing Centre Singapore (NSCC), and force field support from Materials Computation Center of Penn State University.

References

[1] M. Peplow, The race to upcycle CO2 into fuels, concrete and more, Nature 603 (2022) 780–783, https://doi.org/10.1038/d41586-022-00807-y.

[2] T. Watari, Z. Cao, S. Hata, K. Nansai, Efficient use of cement and concrete to reduce reliance on supply-side technologies for net-zero emissions, Nat. Commun. 13 (2022) 1–9, https://doi.org/10.1038/s41467-022-31806-2.

[3] L.M. Seymour, J. Maragh, P. Sabatini, M. Di Tommaso, J.C. Weaver, A. Masic, Hot mixing: mechanistic insights into the durability of ancient Roman concrete, Sci. Adv. 9 (2023) eadd1602, https://doi.org/10.1126/sciadv.add1602.

[4] D.Y. Yoo, N. Banthia, High-performance strain-hardening cementitious composites with tensile strain capacity exceeding 4%: a review, Cem. Concr. Compos. 125 (2022) 104325, https://doi.org/10.1016/j.cemconcomp.2021.104325.

[5] J. Xue, B. Briseghella, F. Huang, C. Nuti, H. Tabatabai, B. Chen, Review of ultra-high performance concrete and its application in bridge engineering, Constr. Build. Mater. 260 (2020) 119844, https://doi.org/10.1016/j.conbuildmat.2020.119844.

[6] X. Sun, Z. Gao, P. Cao, C. Zhou, Mechanical properties tests and multiscale numerical simulations for basalt fiber reinforced concrete, Constr. Build. Mater. 202 (2019) 58–72, https://doi.org/10.1016/j.conbuildmat.2019.01.018.

[7] J. Gong, Y. Ma, J. Fu, J. Hu, X. Ouyang, Z. Zhang, H. Wang, Utilization of fibers in ultra-high performance concrete: a review, Compos. Part B Eng. 241 (2022) 109995, https://doi.org/10.1016/j.compositesb.2022.109995.

[8] B.T. Huang, K.F. Weng, J.X. Zhu, Y. Xiang, J.G. Dai, V.C. Li, Engineered/strain-hardening cementitious composites (ECC/SHCC) with an ultra-high compressive strength over 210 MPa, Compos. Commun. 26 (2021) 100775, https://doi.org/10.1016/j.coco.2021.100775.

[9] D. Zhang, J. Yu, H. Wu, B. Jaworska, B.R. Ellis, V.C. Li, Discontinuous micro-fibers as intrinsic reinforcement for ductile engineered cementitious composites (ECC), Compos. Part B Eng. 184 (2020) 107741, https://doi.org/10.1016/j.compositesb.2020.107741.

[10] Z. Wang, G. Ma, Z. Ma, Y. Zhang, Flexural behavior of carbon fiber-reinforced concrete beams under impact loading, Cem. Concr. Compos. 118 (2021) 103910, https://doi.org/10.1016/j.cemconcomp.2020.103910.

[11] W. Meng, K.H. Khayat, Effect of graphite nanoplatelets and carbon nanofibers on rheology, hydration, shrinkage, mechanical properties, and microstructure of UHPC, Cem. Concr. Res. 105 (2018) 64–71, https://doi.org/10.1016/j.cemconres.2018.01.001.

[12] S.L. Xu, H.L. Xu, B.T. Huang, Q.H. Li, K.Q. Yu, J.T. Yu, Development of ultrahigh-strength ultrahigh-toughness cementitious composites (UHS-UHTCC) using polyethylene and steel fibers, Compos. Commun. 29 (2022) 100992, https://doi.org/10.1016/j.coco.2021.100992.

[13] C. Xie, M. Cao, M. Khan, H. Yin, J. Guan, Review on different testing methods and factors affecting fracture properties of fiber reinforced cementitious composites, Constr. Build. Mater. 273 (2021) 121766, https://doi.org/10.1016/j.conbuildmat.2020.121766.

[14] D. Zhu, S. Liu, Y. Yao, G. Li, Y. Du, C. Shi, Effects of short fiber and pre-tension on the tensile behavior of basalt textile reinforced concrete, Cem. Concr. Compos. 96 (2019) 33–45, https://doi.org/10.1016/j.cemconcomp.2018.11.015.

[15] T.V. Muthukumarana, M.A.V.H.M. Arachchi, H.M.C.C. Somarathna, S.N. Raman, A review on the variation of mechanical properties of carbon fibre-reinforced concrete, Constr. Build. Mater. 366 (2023) 130173, https://doi.org/10.1016/j.conbuildmat.2022.130173.

[16] S. Pirmohammad, Y. Majd Shokorlou, B. Amani, Laboratory investigations on fracture toughness of asphalt concretes reinforced with carbon and kenaf fibers, Eng. Fract. Mech. 226 (2020) 106875, https://doi.org/10.1016/j.engfracmech.2020.106875.

[17] M. Monazami, R. Gupta, Investigation of mechanical behavior and fracture energy of fiber-reinforced concrete beams and panels, Cem. Concr. Compos. 133 (2022) 104656, https://doi.org/10.1016/j.cemconcomp.2022.104656.

[18] M.R.M. Aliha, H. Reza Karimi, M. Abedi, The role of mix design and short glass fiber content on mode-I cracking characteristics of polymer concrete, Constr. Build. Mater. 317 (2022) 126139, https://doi.org/10.1016/j.conbuildmat.2021.126139.

[19] K.L. Scrivener, A.K. Crumbie, P. Laugesen, The interfacial transition zone (ITZ) between cement paste and aggregate in concrete, Interface Sci. 12 (2004) 411–421, https://doi.org/10.1023/B:INTS.0000042339.92990.4c.

[20] Y. Gao, X. Zhu, D.J. Corr, M.S. Konsta-Gdoutos, S.P. Shah, Characterization of the interfacial transition zone of CNF-reinforced cementitious composites, Cem. Concr. Compos. 99 (2019) 130–139, https://doi.org/10.1016/j.cemconcomp.2019.03.002.

[21] Y. Gan, H. Zhang, M. Liang, Y. Zhang, E. Schlangen, K. van Breugel, B. Šavija, Flexural strength and fatigue properties of interfacial transition zone at the microscale, Cem. Concr. Compos. 133 (2022) 104717, https://doi.org/10.1016/j.cemconcomp.2022.104717.

[22] M.R.M. Aliha, D.M. Imani, S.M. Salehi, M. Shojaee, M. Abedi, Mixture optimization of epoxy base concrete for achieving highest fracture toughness and fracture energy values using taguchi method, Compos. Commun. 32 (2022) 101150, https://doi.org/10.1016/j.coco.2022.101150.

[23] A. Picker, L. Nicoleau, Z. Burghard, J. Bill, I. Zlotnikov, C. Labbez, A. Nonat, H. Cölfen, Mesocrystalline calcium silicate hydrate: a bioinspired route toward elastic concrete materials, Sci. Adv. 3 (2017) e1701216.

[24] L. Yu, R. Wu, Using graphene oxide to improve the properties of ultra-high-performance concrete with fine recycled aggregate, Constr. Build. Mater. 259 (2020) 120657, https://doi.org/10.1016/j.conbuildmat.2020.120657.

[25] B.L. Rajput, S.S. Pimplikar, Application of nanomaterials in concrete – a review, J. Adv. Res. Dyn. Control Syst. 10 (2018) 1509–1513, https://doi.org/10.1515/NTREV-2020-0107/ASSET/GRAPHIC/J_NTREV-2020-0107_FIG_009.JPG.

[26] J. Wang, X. Wang, S. Ding, A. Ashour, F. Yu, X. Lv, B. Han, Micro-nano scale pore structure and fractal dimension of ultra-high performance cementitious composites modified with nanofillers, Cem. Concr. Compos. 141 (2023) 105129, https://doi.org/10.1016/j.cemconcomp.2023.105129.

[27] K. Cui, J. Chang, Hydration, reinforcing mechanism, and macro performance of multi-layer graphene-modified cement composites, J. Build. Eng. 57 (2022) 104880, https://doi.org/10.1016/j.jobe.2022.104880.

[28] Q. Fu, Z. Zhou, Z. Wang, J. Huang, D. Niu, Insight into dynamic compressive response of carbon nanotube/carbon fiber-reinforced concrete, Cem. Concr. Compos. 129 (2022) 104471, https://doi.org/10.1016/j.cemconcomp.2022.104471.

[29] S. Dong, Y. Wang, A. Ashour, B. Han, J. Ou, Nano/micro-structures and mechanical properties of ultra-high performance concrete incorporating graphene with different lateral sizes, Compos. Part A Appl. Sci. Manuf. 137 (2020) 106011, https://doi.org/10.1016/j.compositesa.2020.106011.

[30] L. Yu, S. Bai, X. Guan, Effect of graphene oxide on microstructure and micromechanical property of ultra-high performance concrete, Cem. Concr. Compos. 138 (2023) 104964, https://doi.org/10.1016/j.cemconcomp.2023.104964.

[31] C. Liu, X. Hunag, Y.Y. Wu, X. Deng, Z. Zheng, B. Yang, Studies on mechanical properties and durability of steel fiber reinforced concrete incorporating graphene oxide, Cem. Concr. Compos. 130 (2022) 104508, https://doi.org/10.1016/J.CEMCONCOMP.2022.104508.

[32] P. Chindaprasirt, P. Sukontasukkul, A. Techaphatthanakon, S. Kongtun, C. Ruttanapun, D.Y. Yoo, W. Tangchirapat, S. Limkatanyu, N. Banthia, Effect of graphene oxide on single fiber pullout behavior, Constr. Build. Mater. 280 (2021) 122539, https://doi.org/10.1016/J.CONBUILDMAT.2021.122539.

[33] Q. Luo, Y.Y. Wu, W. Qiu, H. Huang, S. Pei, P. Lambert, D. Hui, Improving flexural strength of UHPC with sustainably synthesized graphene oxide, Nanotechnol. Rev. 10 (2021) 754–767, https://doi.org/10.1515/ntrev-2021-0050.

[34] L. Yang, Z. Zhu, D. Zhang, H. Sun, W. Huo, J. Zhang, Y. Wan, C. Zhang, Influence mechanism of Nano-SiO2 on geopolymer recycled concrete: change mechanism of the microstructure and the anti-carbonation mechanism, Cem. Concr. Compos. 146 (2024) 105364, https://doi.org/10.1016/J.CEMCONCOMP.2023.105364.

[35] J. Liu, W. Zhao, L. Li, Effects of Nano-SiO2 grafting on improving the interfacial and mechanical properties of concrete with rice straw fibers, Constr. Build. Mater. 398 (2023) 132516, https://doi.org/10.1016/J.CONBUILDMAT.2023.132516.

[36] M. Garg, C.S. Das, R. Gupta, Use of silica particles to improve dispersion of -COOH CNTs/carbon fibers to produce HyFRCC, Constr. Build. Mater. 250 (2020) 118777, https://doi.org/10.1016/J.CONBUILDMAT.2020.118777.

[37] M. Khan, M. Cao, C. Xie, M. Ali, Efficiency of basalt fiber length and content on mechanical and microstructural properties of hybrid fiber concrete, Fatigue Fract. Eng. Mater. Struct. 44 (2021) 2135–2152, https://doi.org/10.1111/ffe.13483.

[38] B. Şimşek, T. Uygunoğlu, Synergistic effect of nanoparticles and super absorbent polymer on self-healing ability of cement pastes, Compos. Commun. 34 (2022) 101279, https://doi.org/10.1016/j.coco.2022.101279.

[39] L. Guo, J. Wu, H. Wang, Mechanical and perceptual characterization of ultra-high-performance cement-based composites with silane-treated graphene nano-platelets, Constr. Build. Mater. 240 (2020) 117926, https://doi.org/10.1016/j.conbuildmat.2019.117926.

[40] J. Fu, S. Kamali-Bernard, F. Bernard, M. Cornen, Comparison of mechanical properties of C-S-H and portlandite between nano-indentation experiments and a modeling approach using various simulation techniques, Compos. Part B Eng. 151 (2018) 127–138, https://doi.org/10.1016/j.compositesb.2018.05.043.

[41] J. Fu, F. Bernard, S. Kamali-Bernard, Assessment of the elastic properties of amorphous calcium silicates hydrates (I) and (II) structures by molecular dynamics simulation, Mol. Simul. 44 (2018) 285–299, https://doi.org/10.1080/08927022.2017.1373191.

[42] G. Constantinides, F.J. Ulm, The effect of two types of C-S-H on the elasticity of cement-based materials: results from nanoindentation and micromechanical modeling, Cem. Concr. Res. 34 (2004) 67–80, https://doi.org/10.1016/S0008-8846(03)00230-8.

[43] M. Bauchy, H. Laubie, M.J. Abdolhosseini Qomi, C.G. Hoover, F.J. Ulm, R.J. M. Pellenq, Fracture toughness of calcium-silicate-hydrate from molecular dynamics simulations, J. Non. Cryst. Solids. 419 (2015) 58–64, https://doi.org/10.1016/j.jnoncrysol.2015.03.031.

[44] Y. Zhang, S. Zhang, X. Jiang, Q. Chen, Z. Jiang, J.W. Ju, M. Bauchy, Insights into the thermal effect on the fracture toughness of calcium silicate hydrate grains: a reactive molecular dynamics study, Cem. Concr. Compos. 134 (2022) 104824, https://doi.org/10.1016/j.cemconcomp.2022.104824.

[45] Y. Yang, Y. Wang, J. Cao, Prediction and evaluation of thermal conductivity in nanomaterial-reinforced cementitious composites, Cem. Concr. Res. 172 (2023) 107240, https://doi.org/10.1016/J.CEMCONRES.2023.107240.

[46] Y. Zhou, C. Xiong, Z. Peng, J. Huang, H. Chang, Molecular dynamics simulation of the interfacial interaction mechanism between functional groups on graphene-based two-dimensional matrix and calcium silicate hydrate, Constr. Build. Mater. 284 (2021) 122804, https://doi.org/10.1016/J.CONBUILDMAT.2021.122804.

[47] A.A. Bahraq, M.A. Al-Osta, I.B. Obot, O.S. Baghabra Al-Amoudi, T.A. Saleh, M. Maslehuddin, Improving the adhesion properties of cement/epoxy interface using graphene-based nanomaterials: insights from molecular dynamics simulation, Cem. Concr. Compos. 134 (2022) 104801, https://doi.org/10.1016/J.CEMCONCOMP.2022.104801.

[48] V. Varshney, S.S. Patnaik, A.K. Roy, B.L. Farmer, A molecular dynamics study of epoxy-based networks: cross-linking procedure and prediction of molecular and material properties, Macromolecules 41 (2008) 6837–6842, https://doi.org/10.1021/ma801153e.

[49] Z. Liu, J. Li, C. Zhou, W. Zhu, A molecular dynamics study on thermal and rheological properties of BNNS-epoxy nanocomposites, Int. J. Heat Mass Transf. 126 (2018) 353–362, https://doi.org/10.1016/j.ijheatmasstransfer.2018.05.149.

[50] F. Liu, Z. Shi, Y. Dong, Improved wettability and interfacial adhesion in carbon fibre/epoxy composites via an aqueous epoxy sizing agent, Compos. Part A Appl. Sci. Manuf. 112 (2018) 337–345, https://doi.org/10.1016/j.compositesa.2018.06.026.

[51] S. Yu, S. Yang, M. Cho, Multi-scale modeling of cross-linked epoxy nanocomposites, Polymer (guildf). 50 (2009) 945–952, https://doi.org/10.1016/j.polymer.2008.11.054.

[52] S.D. Gardner, C.S.K. Singamsetty, G.L. Booth, G.R. He, C.U. Pittman, Surface characterization of carbon fibers using angle-resolved XPS and ISS, Carbon N. Y. 33 (1995) 587–595, https://doi.org/10.1016/0008-6223(94)00144-O.

[53] J. Li, Y. Huang, Z. Xu, Z. Wang, High-energy radiation technique treat on the surface of carbon fiber, Mater. Chem. Phys. 94 (2005) 315–321, https://doi.org/10.1016/j.matchemphys.2005.05.007.

[54] H. Wang, K. Jin, C. Wang, X. Guo, Z. Chen, J. Tao, Effect of fiber surface functionalization on shear behavior at carbon fiber/epoxy interface through molecular dynamics analysis, Compos. Part A Appl. Sci. Manuf. 126 (2019) 105611, https://doi.org/10.1016/j.compositesa.2019.105611.

[55] S.A. Hamid, The crystal structure of the 11 Ä natural tobermorite ca 2.25 [si 3 O 7.5 (OH) 1.5]·1H 2 O, Zeitschrift Für Krist. - Cryst. Mater. 154 (1981) 189–198, https://doi.org/10.1524/zkri.1981.154.14.189.

[56] A. Ayuela, J.S. Dolado, I. Campillo, Y.R. De Miguel, E. Erklzia, D. Sánchez-Portal, A. Rubio, A. Porro, P.M. Echenique, Silicate chain formation in the nanostructure of cement-based materials, J. Chem. Phys. 127 (2007) 164710, https://doi.org/10.1063/1.2796171.

[57] I.G. Richardson, Nature of C-S-H in hardened cements, Cem. Concr. Res. 29 (1999) 1131–1147, https://doi.org/10.1016/S0008-8846(99)00168-4.

[58] M.J. Abdolhosseini Qomi, K.J. Krakowiak, M. Bauchy, K.L. Stewart, R. Shahsavari, D. Jagannathan, D.B. Brommer, A. Baronnet, M.J. Buehler, S. Yip, F.J. Ulm, K. J. Van Vliet, R.J.M. Pellenq, Combinatorial molecular optimization of cement hydrates, Nat. Commun. 5 (2014) 1–10, https://doi.org/10.1038/ncomms5960.

[59] R.J.M. Pellenq, A. Kushima, R. Shahsavari, K.J. Van Vliet, M.J. Buehler, S. Yip, F. J. Ulm, A realistic molecular model of cement hydrates, Proc. Natl. Acad. Sci. U. S. A. 106 (2009) 16102–16107, https://doi.org/10.1073/pnas.0902180106.

[60] B. Min, P. Wang, S. Li, Z. Wang, Mechanical influence of graphene oxide in the interface between calcium silicate hydrate and quartz: a molecular dynamics study, Constr. Build. Mater. 325 (2022) 126597, https://doi.org/10.1016/j.conbuildmat.2022.126597.

[61] H. Manzano, S. Moeini, F. Marinelli, A.C.T. Van Duin, F.J. Ulm, R.J.M. Pellenq, Confined water dissociation in microporous defective silicates: mechanism, dipole distribution, and impact on substrate properties, J. Am. Chem. Soc. 134 (2012) 2208–2215, https://doi.org/10.1021/ja209152n.

[62] R.T. Cygan, J.A. Greathouse, A.G. Kalinichev, Advances in clayff Molecular simulation of layered and nanoporous materials and their aqueous Interfaces, J. Phys. Chem. C. 125 (2021) 17573–17589, https://doi.org/10.1021/acs.jpcc.1c04600.

[63] R.T. Cygan, J.J. Liang, A.G. Kalinichev, Molecular models of hydroxide, oxyhydroxide, and clay phases and the development of a general force field, J. Phys. Chem. B. 108 (2004) 1255–1266, https://doi.org/10.1021/jp0363287.

[64] S. Zhu, M.A. Khan, T. Kameda, H. Xu, F. Wang, M. Xia, T. Yoshioka, New insights into the capture performance and mechanism of hazardous metals Cr3+ and Cd2+ onto an effective layered double hydroxide based material, J. Hazard. Mater. 426 (2022) 128062, https://doi.org/10.1016/j.jhazmat.2021.128062.

[65] X. Wang, W. Liu, W. Liu, Y. Shen, H. Duan, J. Qiu, X. Gu, Understanding adsorption of amine surfactants on the solvated quartz (1 0 1) surface by a jointed dreiding-ClayFF force field, Appl. Surf. Sci. 566 (2021) 150737, https://doi.org/10.1016/j.apsusc.2021.150737.

[66] P. Dauber-Osguthorpe, V.A. Roberts, D.J. Osguthorpe, J. Wolff, M. Genest, A. T. Hagler, Structure and energetics of ligand binding to proteins: Escherichia coli dihydrofolate reductase-trimethoprim, a drug-receptor system, Proteins Struct. Funct. Bioinforma. 4 (1988) 31–47, https://doi.org/10.1002/prot.340040106.

[67] B. Yang, Y. Li, S. Wang, R. Nie, Q. Wang, Aminosilane modified graphene oxide for reinforcing nitrile butadiene rubber: Experiments and molecular dynamic simulations, Compos. Sci. Technol. 235 (2023) 109956, https://doi.org/10.1016/j.compscitech.2023.109956.

[68] S.C. Chowdhury, R.M. Elder, T.W. Sirk, J.W. Gillespie, Epoxy resin thermo-mechanics and failure modes: effects of cure and cross-linker length, Compos. Part B Eng. 186 (2020) 107814, https://doi.org/10.1016/j.compositesb.2020.107814.

[69] V. Varshney, S.S. Patnaik, A.K. Roy, B.L. Farmer, Heat transport in epoxy networks: a molecular dynamics study, Polymer (guildf). 50 (2009) 3378–3385, https://doi.org/10.1016/j.polymer.2009.05.027.

[70] F. Sanchez, L. Zhang, Interaction energies, structure, and dynamics at functionalized graphitic structure-liquid phase interfaces in an aqueous calcium sulfate solution by molecular dynamics simulation, Carbon N. Y. 48 (2010) 1210–1223, https://doi.org/10.1016/j.carbon.2009.11.044.

[71] O. Büyüköztürk, M.J. Buehler, D. Lau, C. Tuakta, Structural solution using molecular dynamics: fundamentals and a case study of epoxy-silica interface, Int. J. Solids Struct. 48 (2011) 2131–2140, https://doi.org/10.1016/j.ijsolstr.2011.03.018.

[72] S. Plimpton, Fast parallel algorithms for short-range molecular dynamics, J. Comput. Phys. 117 (1995) 1–19, https://doi.org/10.1006/jcph.1995.1039.

[73] A. Stukowski, Visualization and analysis of atomistic simulation data with OVITO-the open visualization tool, Model. Simul. Mater. Sci. Eng. 18 (2010) 015012, https://doi.org/10.1088/0965-0393/18/1/015012.

[74] W. Humphrey, A. Dalke, K. Schulten, VMD: visual molecular dynamics, J. Mol. Graph. 14 (1996) 33–38, https://doi.org/10.1016/0263-7855(96)00018-5.

[75] S. Park, K. Schulten, Calculating potentials of mean force from steered molecular dynamics simulations, J. Chem. Phys. 120 (2004) 5946–5961, https://doi.org/10.1063/1.1651473.

[76] T. Lu, F. Chen, Multiwfn: a multifunctional wavefunction analyzer, J. Comput. Chem. 33 (2012) 580–592, https://doi.org/10.1002/jcc.22885.

[77] M.N. Pavlovic, Fracture mechanics of concrete: applications of fracture mechanics to concrete, rock and other quasi-brittle materials, Eng. Struct. 11 (1996) 887–888, https://doi.org/10.1016/0141-0296(96)84816-4.

[78] D. Hou, Q. Yang, Z. Jin, P. Wang, M. Wang, X. Wang, Y. Zhang, Enhancing interfacial bonding between epoxy and CSH using graphene oxide: an atomistic investigation, Appl. Surf. Sci. 568 (2021) 150896, https://doi.org/10.1016/J.APSUSC.2021.150896.

[79] Q. Luo, Y. Li, Z. Zhang, X. Peng, G. Geng, Influence of substrate moisture on the interfacial bonding between calcium silicate hydrate and epoxy, Constr. Build. Mater. 320 (2022) 126252, https://doi.org/10.1016/J.CONBUILDMAT.2021.126252.

[80] Z. Yu, A. Zhou, W. Ning, L. Ho Tam, Molecular insights into the weakening effect of water on cement/epoxy interface, Appl. Surf. Sci. 553 (2021) 149493, https://doi.org/10.1016/J.APSUSC.2021.149493.

[81] Y. Wang, F. Meng, F. Huang, Y. Li, X. Tian, Y. Mei, Z. Zhou, Ultrastrong Carbon nanotubes/graphene papers via multiple πcross-linking, ACS Appl. Mater. Interfaces. 12 (2020) 47811–47819, https://doi.org/10.1021/acsami.0c12501.

[82] T. Namikawa, J. Koseki, Evaluation of tensile strength of cement-treated sand based on several types of laboratory tests, Soils Found. 47 (2007) 657–674, https://doi.org/10.3208/sandf.47.657.

[83] W.W. Li, W.M. Ji, G.H. Fang, Y.Q. Liu, F. Xing, Y.K. Liu, B.Q. Dong, Electrochemical impedance interpretation for the fracture toughness of carbon nanotube/cement composites, Constr. Build. Mater. 114 (2016) 499–505, https://doi.org/10.1016/j.conbuildmat.2016.03.215.

[84] B. Min, X. Chen, K. Li, Z. Wang, Multiscale study of enhancing the fracture properties of interfacial transition zone: insights from molecular dynamics and finite element simulations, Constr. Build. Mater. 409 (2023) 133846, https://doi.org/10.1016/J.CONBUILDMAT.2023.133846.

[85] X. Yao, E. Shamsaei, W. Wang, S. Zhang, K. Sagoe-Crentsil, W. Duan, Graphene-based modification on the interface in fibre reinforced cementitious composites for improving both strength and toughness, Carbon N. Y. 170 (2020) 493–502, https://doi.org/10.1016/J.CARBON.2020.08.051.

[86] S. Yan, P. He, D. Jia, Z. Yang, X. Duan, S. Wang, Y. Zhou, Effect of fiber content on the microstructure and mechanical properties of carbon fiber felt reinforced geopolymer composites, Ceram. Int. 42 (2016) 7837–7843, https://doi.org/10.1016/j.ceramint.2016.01.197.

[87] E. Monaldo, F. Nerilli, G. Vairo, Basalt-based fiber-reinforced materials and structural applications in civil engineering, Compos. Struct. 214 (2019) 246–263, https://doi.org/10.1016/j.compstruct.2019.02.002.

[88] J. Liu, B. Min, Z. Wang, S. Li, Multiscale structure construction by layer-by-layer self-assembly to modify the Carbon fiber Surface, J. Phys. Chem. C. 124 (2020) 10733–10743, https://doi.org/10.1021/acs.jpcc.0c01920.